



# Seasonal dynamics of a permafrost landscape, Adventdalen, Svalbard, investigated by InSAR

Line Rouyet<sup>a,b,c,\*</sup>, Tom Rune Lauknes<sup>a</sup>, Hanne H. Christiansen<sup>c</sup>, Sarah M. Strand<sup>c,d</sup>,  
Yngvar Larsen<sup>a</sup>

<sup>a</sup> NORCE Norwegian Research Centre AS, Siva Innovasjonssenter, P.O. Box 6434, 9294, Tromsø, Norway

<sup>b</sup> Department of Geosciences, The Arctic University of Norway (UiT), P.O. Box 6050, Langnes, 9037, Tromsø, Norway

<sup>c</sup> Arctic Geology Department, The University Centre in Svalbard (UNIS), P.O. Box 156, 9171, Longyearbyen, Norway

<sup>d</sup> Department of Geosciences, University of Oslo (UiO), P.O. Box 1047, Blindern, 0316, Oslo, Norway

## ARTICLE INFO

Edited by Jing M. Chen

**Keywords:**

InSAR  
Permafrost  
Svalbard  
Arctic  
Thaw subsidence  
Frost heave  
Creep  
Periglacial landforms

## ABSTRACT

Nordenskiöld Land in Central Spitsbergen, Svalbard is characterized as a high latitude, high relief periglacial landscape with permafrost occurring both in mountains and lowlands. Freezing and thawing of the active layer causes seasonal frost heave and thaw subsidence, while permafrost-related mass-wasting processes induce downslope ground displacements on valley sides. Displacement rate varies spatially and temporally depending on environmental factors. In our study, we apply Satellite Synthetic Aperture Radar Interferometry (InSAR) to investigate the magnitude, spatial distribution and timing of seasonal ground displacements in and around Adventdalen using TerraSAR-X StripMap Mode (2009–2017) and Sentinel-1 Interferometric Wide Swath Mode (2015–2017) SAR images. First, we show that InSAR results from both sensors highlight consistent patterns and provide a comprehensive overview of the distribution of displacement rates. Secondly, two-dimensional (2D) TerraSAR-X InSAR results from combined ascending and descending geometries document the spatial variability of the vertical and east-west horizontal displacement rates for an average of nine thawing seasons. The remote sensing results are compared to a simplified geomorphological map enabling the identification of specific magnitudes and orientations of displacements for 14 selected geomorphological units. Finally, June to December 2017 6-day sampling interval Sentinel-1 time series was retrieved and compared to active layer ground temperatures from two boreholes. The timing of the subsidence and heave detected by InSAR matches the thawing and freeze-back periods measured by in-situ sensors. Our results highlight the value of InSAR to obtain landscape scale knowledge about the seasonal dynamics of complex periglacial environments.

## 1. Introduction

Permafrost is defined as subground material remaining at or below 0 °C for at least two consecutive years (French, 2007). It exists in approximately 24% of the terrestrial land areas of the Northern Hemisphere (Zhang et al., 2003). The uppermost part of the ground above the permafrost, which thaws in summer and refreezes in winter, is the active layer (Shur et al., 2005). During this seasonal freezing and thawing, the water-ice phase change in the ground can induce cm-scale heave and subsidence (Harris et al., 2011; Romanovsky et al., 2008). The magnitude of such displacements varies spatially depending on the active layer thickness (ALT), the amount and availability of water and the frost-susceptibility of the ground, which is largely controlled by grain size (Harris et al., 1995; Matsuoka et al., 2003; Zhang and

Michalowski, 2015). On slopes, mass-wasting processes create various creeping landforms (e.g. rock glaciers, solifluction lobes/sheets) depending on climate, topography, ground material, water content, etc. (Haeberli et al., 2006; Matsuoka, 2001).

Climate change impacts the properties and distribution of frozen ground (Nelson et al., 2002), and changes of the ground thermal regime can modify the distribution, magnitude and timing of ground heave, subsidence and creep. Moreover, the seasonal freeze/thaw cycles affect slope stability (Blikra and Christiansen, 2014) and infrastructure (Harris et al., 2009). Thus, measuring ground dynamics in permafrost landscapes is important. Various monitoring networks exist that document ALT (Shiklomanov et al., 2012), permafrost thermal state (Romanovsky et al., 2010) and creep behaviour in rock glaciers (Delaloye et al., 2010), but these measurements are typically sparse and

\* Corresponding author at: NORCE Norwegian Research Centre AS, P.O. Box 6434, Siva Innovasjonssenter, 9294 Tromsø, Norway.

E-mail address: [line.rouyet@norce-research.no](mailto:line.rouyet@norce-research.no) (L. Rouyet).

<https://doi.org/10.1016/j.rse.2019.111236>

Received 2 October 2018; Received in revised form 29 May 2019; Accepted 1 June 2019

Available online 19 June 2019

0034-4257/ © 2019 The Authors. Published by Elsevier Inc. This is an open access article under the CC BY-NC-ND license

(<http://creativecommons.org/licenses/by-nc-nd/4.0/>).

unevenly distributed.

Satellite remote sensing provides a valuable tool to explore large and hard-to-access periglacial areas, allowing the Earth's surface to be imaged at high spatial and temporal resolution. Permafrost, as a sub-surface condition, cannot be directly observed from satellites, but its impact on the surface can be documented by remote sensing (Bartsch et al., 2016; Trofaier et al., 2017). The use of Synthetic Aperture Radar (SAR) satellites is especially suitable in the Arctic as SAR imaging is independent of solar insolation and meteorological conditions. Repeat-pass Differential SAR Interferometry (InSAR) can detect ground displacements at millimetre to centimetre scales along the radar line-of-sight (LOS) and has been proven valuable for geoscience applications (Gabriel et al., 1989; Massonnet and Feigl, 1998).

InSAR in permafrost landscapes can measure creep on slopes and heave/subsidence in low-relief areas. Kenyi and Kaufmann (2001) and Rignot et al. (2002) used InSAR to measure rock glacier surface motion. Recent studies exploited the regional coverage of SAR satellites for inventorying creeping landforms (Barboux et al., 2014, 2015; Delaloye et al., 2007; Strozzi et al., 2004) or investigating temporal variations of velocity using long time series (Strozzi et al., 2010; Eriksen et al., 2018). The first cases of vertical seasonal displacements detected by InSAR in Alaska were documented by Rykhus and Lu (2008) and Wang and Li (1999). InSAR has then been used to map seasonal thaw subsidence, to identify terrain stability issues (Short et al., 2014; Wang et al., 2017; Wolfe et al., 2014) and to estimate ALT over large areas (Liu et al., 2012; Schaefer et al., 2015). Recent research modelled the relationship between InSAR displacements and climatic factors (Zhao et al., 2016), evidenced the importance of ground water content (Daout et al., 2017) and documented the inter-annual ground surface changes (Rudy et al., 2018; Strozzi et al., 2018). These studies show that InSAR is a promising technique for documenting slope movement processes and studying seasonal landscape dynamics related to ground freezing and thawing. However, little research has focused on landscapes combining high-relief and lowland permafrost-related processes. The capability of InSAR to inventory individual landforms based on their displacement patterns, and to contribute to geomorphological investigation in such complex environments, still needs to be investigated.

Here we study to what degree InSAR can identify seasonal frost- and thaw-related ground displacements in Svalbard. Based on pre-existing InSAR techniques, the novelty of our study is to combine the spatial and temporal measurement capability of complementary SAR datasets to provide new insights into the seasonal dynamics of the Svalbard landscape. Our study objectives are to (1) analyse the spatial distribution of 2D InSAR results documenting thaw subsidence and creep at the landscape scale, and study the variability of the displacement patterns for different geomorphological units; (2) investigate the temporal variations in InSAR displacements and compare the results to in situ ALT ground temperature measurements; (3) discuss the complementarity of two SAR sensors and the value of Sentinel-1 for studies of periglacial landscape dynamics.

## 2. Study area

The study area is centred in Adventdalen valley and adjacent parts of central Nordenskiöld Land, on the Spitsbergen Island, in the Svalbard archipelago (Fig. 1). The landscape has complex topography with mountain tops over 1000 m a.s.l. and glacially eroded – now periglacially dominated – valleys extending down to sea level (Norwegian Polar Institute, 2014a). The large-scale geomorphology is dominated by mountain plateaus with a sub-horizontal stratification of sedimentary bedrock (Dallmann et al., 2001; Major et al., 2001).

Following regional deglaciation, the landscape has been modified by weathering, local glaciation and periglacial processes (Gilbert et al., 2018; Härtel and Christiansen, 2014; Sørbel et al., 2001; Tolgensbakk et al., 2001). Bedrock is exposed mainly on rock noses in the upper

steep part of the slopes composed of the resistant Firkanten formation of Tertiary sediments (Dallmann et al., 2001; Major et al., 2001). The plateaus are covered by extensive blockfields. The lower and central parts of Adventdalen and the neighbouring valleys (Fig. 1, right) are characterized by fluvial, alluvial and eolian (loess) deposits with typical permafrost-related landforms, such as ice-wedge polygons and pingos (Sørbel et al., 2001). The valley slopes are covered by allochthonous weathered material, colluvium and alluvial fans, that have been further reworked by mass-wasting processes, such as by debris-flows (André, 1995), solifluction (Harris et al., 2011), snow avalanche activity (Eckerstorfer et al., 2013), and talus-derived rock glaciers (Humlum, 2000).

Svalbard is characterized by a polar-tundra climate (Köppen–Geiger classification, Peel et al., 2007) and has continuous permafrost with a thickness varying from < 100 m in valley bottoms and coastal areas to 500 m in the mountains (Humlum et al., 2003). Gilbert et al. (2018) highlighted the complex Holocene history of sedimentary infilling and permafrost aggradation in Adventdalen, suggesting that permafrost is predominantly epigenetic. Considering the period 1912–2011, air temperature records show an increase by 2.5 °C at the Svalbard airport meteorological station. During the last decades, the average increase reached 1.0–1.2 °C per decade, but 2–3 °C per decade during the winter season (Førland et al., 2011). Ground temperature monitoring in boreholes since 2008 indicates that the permafrost has warmed from 0.06 to 0.15 °C/year (Isaksen et al., 2019). ALT increased by 0.6 cm/year in lower Adventdalen (UNISCALM monitoring site) based on 2000–2017 measurements (Isaksen et al., 2019). Modelling for the twenty-first century suggests future increases of ground temperatures and ALT (Etzelmueller et al., 2011; Isaksen et al., 2019). However, the intra- and inter-annual meteorological variability, as well as the influence of local conditions (water content, ground characteristics, snow cover, vegetation) are not negligible (Christiansen and Humlum, 2008; Christiansen et al., 2013; Harris et al., 2011; Schuh et al., 2017). ALT is generally in the range of 100 to 200 cm (Isaksen et al., 2019) and the amount of ice in the upper permafrost has high spatial variability (Cable et al., 2018; Christiansen et al., 2010).

The study area corresponds to the overlap of the available SAR datasets and the geomorphological map (see Section 3). The processed SAR areas were chosen to maximize the comparable area. The north-eastern part of the geomorphological map is not covered by the TerraSAR-X scenes in ascending geometry leading to a slightly reduced overlap area (Fig. 1, right). The size of the geomorphologically mapped area is approximately 331 km<sup>2</sup>, and the overlap area is about 297 km<sup>2</sup>.

## 3. Data and methods

### 3.1. SAR data

SAR datasets from the TerraSAR-X (TSX) satellite (2009–2017) and the Sentinel-1 (S1) satellites of the European Union's Copernicus Programme (2015–2017) were used to compare the results and to exploit their complementary radar wavelengths, spatial coverages, spatial resolutions, revisit times and data availability. We selected snow-free scenes from TSX in StripMap (SM) mode in ascending and descending geometries, and from S1 in Interferometric Wide Swath (IWS) mode in ascending geometry only (before 2018, IWS mode in descending geometry was not available over Svalbard). Characteristics of the datasets are further described in Table 1.

### 3.2. InSAR processing

InSAR results were obtained using the NORCE GSAR software (Larsen et al., 2005). Parameters used for InSAR processing are summarized in Table S1 (Supplementary material). We co-registered and multi-looked single-look complex (SLC) images using a range/azimuth multi-looking factor of 5 × 5 (TSX) and 8 × 2 (S1), providing a ground

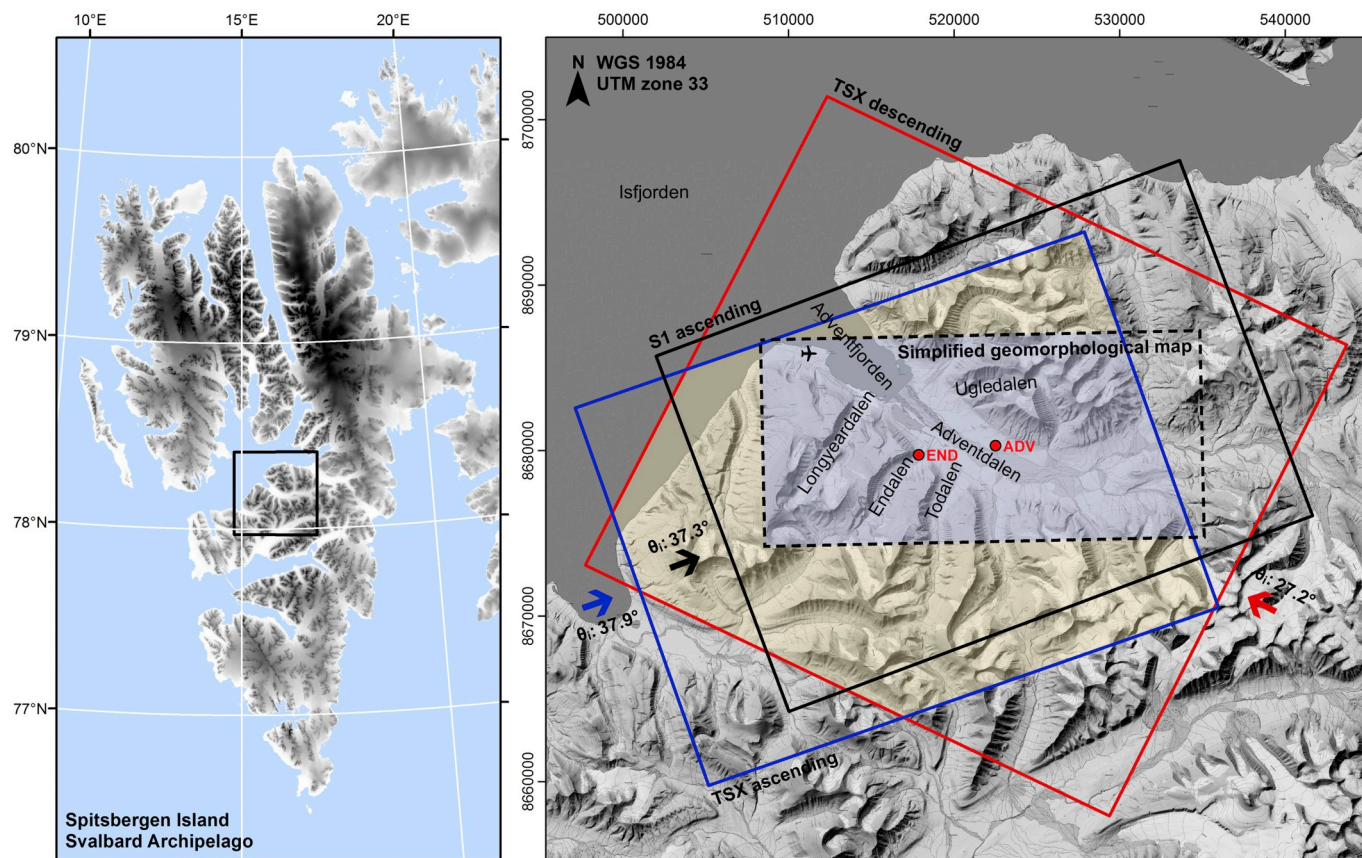


**Fig. 1.** Left: Location of the study area on Spitsbergen Island in the Svalbard archipelago. Black square: extent of the map shown in the right part of the figure. Right: Extent of the processed areas and the geomorphological map (blue rectangle: TerraSAR-X ascending; red rectangle: TerraSAR-X descending; solid black rectangle: Sentinel-1 ascending; dashed black rectangle: simplified geomorphological map). The common area of both TerraSAR-X geometries is shown in light yellow. The overlap with the geomorphological map is shown in light blue. The arrows indicate the line-of-sight (LOS) orientations (label  $\theta_i$ ; incidence angles). The red dots mark the location of two boreholes continuously monitoring ground temperature (ADV: Adventdalen, END: Endalen). Backgrounds: shaded relief from 20 m resolution Digital Elevation Model (Norwegian Polar Institute, 2014a) and topographical map (Norwegian Polar Institute, 2014b). (For interpretation of the references to colour in this figure legend, the reader is referred to the web version of this article.)

resolution of approximately  $15 \times 15$  m (TSX) and  $40 \times 40$  m (S1). Due to the large variety of processes under study and the high velocity expected on several landforms (e.g. rock glaciers, debris-covered glaciers), interferograms were generated with a maximal temporal baseline of 22 days (TSX) and 24 days (S1) to preserve coherence and minimize phase ambiguities. Aliasing occurs when the displacement rate exceeds a quarter of the wavelength during the time interval of the generated interferograms, i.e. 0.78 cm in 11–22 days for TSX and 1.39 cm in 6–24 days for S1. The detectable LOS velocities in this specific study are thus 0.4–0.7 mm/day for TSX and 0.6–2.3 mm/day for S1. The spatial baseline has not been restricted; the effective maximal values being clearly under the critical baseline limit (Table S1, column 4). For TSX, the interferogram stacks in both geometries include SAR combinations during the thawing periods (June to September

2009–2017). For S1, we focused on two different periods, processed using different InSAR methods (Table S1, column 2). First, we included SAR combinations during the thawing periods (June–September 2015–2017) for comparison with TSX results. Secondly, we used scenes from June to December 2017 to document the thawing period (June to October) and the start of the freezing period (October to December). We ended the series in December because snowfall later in winter leads to decorrelation. The noise-level was reduced in all interferograms by applying a spatially adaptive coherence-dependent Goldstein filter (Goldstein and Werner, 1998; Baran et al., 2003). Strongly decorrelated interferograms were removed and pixels affected by layover were masked out. The contribution from the stratified atmosphere was mitigated by a data driven approach where we fit a linear relation between residual phase and topography (Cavalié et al., 2007) using a

**Table 1**  
Characteristics of SAR datasets from TerraSAR-X and Sentinel-1 satellites.

SAR sensor	SAR mode/geometry	Frequency band	Revisit time	Number of selected scenes	Observation period (first–last selected scenes)	LOS (orientation/incidence angle)
TerraSAR-X	StripMap (SM) Ascending	X ( $\lambda$ : 3.11 cm)	11 days	67	22.08.2009–28.09.2017	70.9° 37.9°
TerraSAR-X	StripMap (SM) Descending	X ( $\lambda$ : 3.11 cm)	11 days	65	14.07.2009–03.10.2017	297.5° 27.2°
Sentinel-1	Interferometric Wide Swath (IWS) Ascending	C ( $\lambda$ : 5.55 cm)	12 days until 25.09.2016 6 days after	46	14.08.2015–01.12.2017	69.5° 37.3°

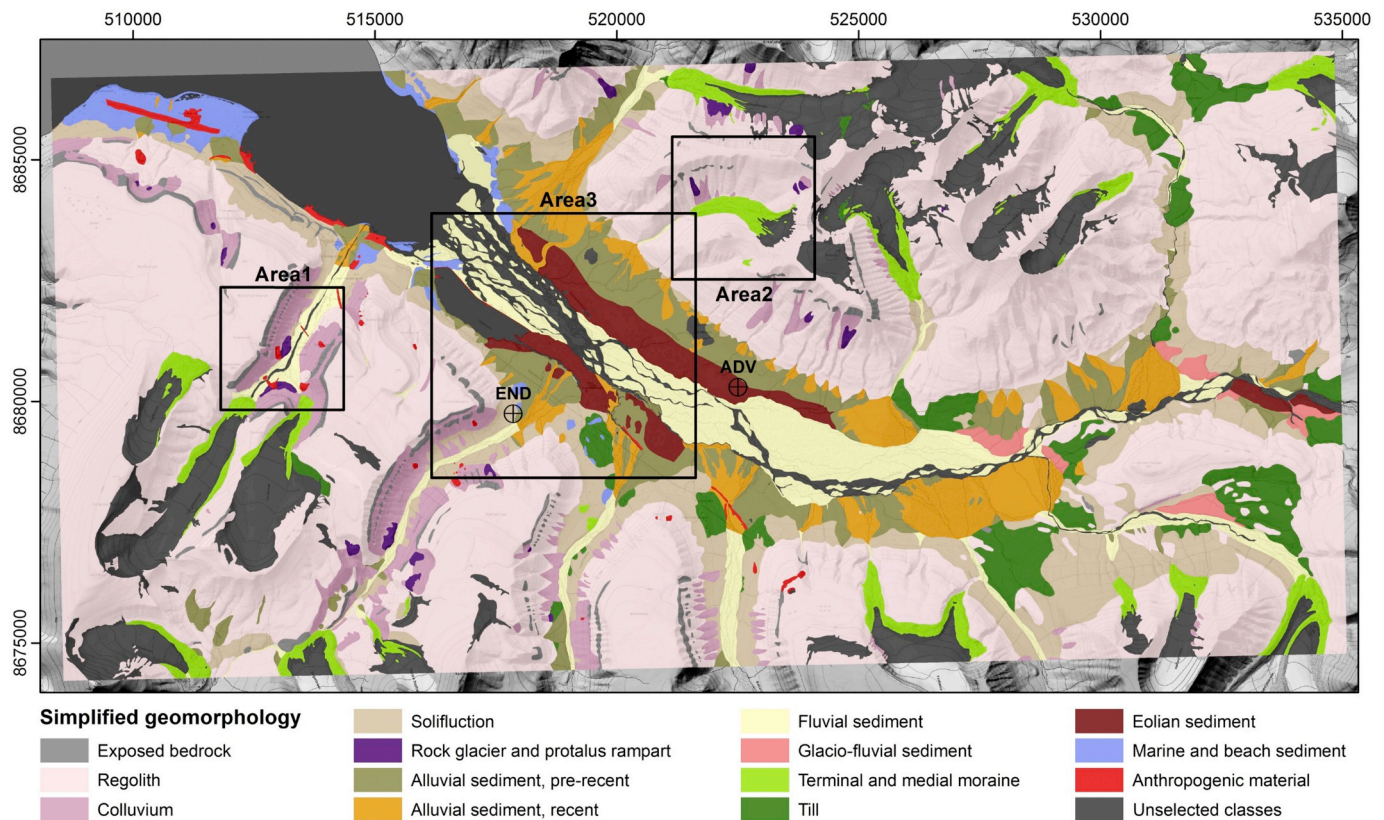


**Fig. 2.** Simplified geomorphological map. Based on map from Hartel and Christiansen (2014) and Tolgensbakk et al. (2001). Black squares indicate the location of the areas shown in Fig. 4. The black crossed circles mark the location of two boreholes (ADV: Adventdalen, END: Endalen). Background: topographical map (Norwegian Polar Institute, 2014b). Location of the 3000 selected InSAR pixels per geomorphological unit is shown in Fig. S5 (Supplementary material).

Digital Elevation Model (DEM) at 20 m resolution (Norwegian Polar Institute, 2014a). Based on a redundant set of interferograms, we further solved for the stratified delay per scene using a network-based approach (Lauknes, 2011). Pixels affected by noise were removed by applying a coherence filter (coherence above 0.3–0.48 in 50% of the interferograms depending on the dataset, Table S1, column 6). The interferograms were unwrapped using the SNAPHU software (Chen and Zebker, 2002) and we performed a second manual quality check of the unwrapped interferograms to remove those affected by major unwrapping errors. For the S1 processing based only on June to December 2017 scenes, we additionally corrected the interferograms by averaging all pairs centred on common acquisitions and using the redundancy to iteratively estimate the atmospheric contribution of each scene (Tymofeyeva and Fialko, 2015). Different reference points were tested and a common reference for all datasets was chosen in an area assumed to be stable on the main building of Svalbard airport (Table S1, column 7; black star in Figs. 3, 5 and 6). All InSAR results are spatially relative to this reference point. Sets of 71–99 selected interferograms, depending on the dataset, were used to retrieve ground displacement information (Table S1, column 5 and Figs. S1–S4 in Supplementary material).

Using maximal temporal baselines of 22 days (TSX) and 24 days (S1), the multi-year datasets include gaps during the winter periods. To take advantage of the large stacks of interferograms from disconnected subsets, we applied a multi-year averaging technique (stacking) based on interferograms from the thawing periods (2009–2017 for TSX and 2015–2017 for S1). The applied stacking is a simple averaging of all selected interferograms weighted by the temporal intervals between the scenes. InSAR stacking reduces the atmospheric effects, assuming temporally uncorrelated tropospheric effects (Lyons and Sandwell, 2003; Peltzer et al., 2001; Sandwell and Price, 1998). Using S1 interferograms, we selected a temporally connected set of interferograms

between June–December 2017 and we estimated displacement time series using the Small Baseline Subset (SBAS) method (Berardino et al., 2002). The phase inversion was performed using a L1-norm-based cost function, which is more robust than L2-norm with respect to unwrapping errors (Lauknes et al., 2011). For the atmospheric filtering, we used a spatial filter of 500 m spatial filter and a temporal filter of 12 days. All results were geocoded using a DEM at 20 m resolution (Norwegian Polar Institute, 2014a).

InSAR stacking results for each dataset (TSX ascending, TSX descending, S1 ascending) correspond to one-dimensional (1D) displacement rates along the LOS (Table 1, column 7), based on several years. All maps based on stacking results highlight the average multi-year displacement rates during the 4-month thawing periods (June–September), expressed in mm/summer. The results from ascending and descending geometries were combined to estimate 2-dimensional (2D) vectors in the plane spanned by the ascending and descending LOS directions (Eriksen et al., 2017). The results were decomposed into vertical (upwards-downwards) and horizontal (eastwards-westwards, E-W) components. 2D InSAR results were retrieved for TSX dataset only, due to unavailability of S1 IWS in descending geometry before 2018. It should be noted that the radar is still blind to movement orthogonal to the LOS plane, which leads to an underestimation of the displacement rates in case of a large horizontal component in the north-south (N-S) direction. To avoid misinterpretation when comparing InSAR to geomorphology, we masked out pixels in areas where a significant horizontal component towards N or S is expected (Eckerstorfer et al., 2018). The mask consists of areas with slope angles over 5° and azimuth angles  $\pm 22.5^\circ$  around 360° (N) and 180° (S) (337.5–22.5° and 157.5–202.5°). All areas with slope angles below 5° were included assuming that they are mainly affected by vertical displacements. To keep a large amount of pixels for the comparison between InSAR and geomorphology, we included areas with NE, NW, SE and SW aspects

**Table 2**  
Information about boreholes, their monitoring instrumentation and the temperature data used in this study.

Borehole	Coordinates (UTM 33N) and altitude	Slope angle and orientation	Geomorphological unit	Total depth	Temperature measurements and additional information
ADV	N 8680294 E 522504 16.7 m a.s.l.	0.4° 293.7° (WNW)	Eolian sediment	3 m	Sensor spacing: every ~0.25 m until 2.5 m depth Data logging: every hour Missing data in November–December 2017
END	N 8679744 E 517857 49.6 m a.s.l.	8.0° 85.8° (E)	Solifluction	20 m	Sensor spacing: every ~0.25 m until 10 m depth, every 2–4 m until 20 m Data logging: every 6 h The ground surface has subsided 0.25 m since 2008, exposing the upper sensors closer to the ground.

assuming that they have a significant E-W displacement component. As a drawback, some areas may be affected by underestimation if the displacements also include a significant N-S component.

The S1 SBAS results provide time series of LOS displacements temporally relative to the first scene of the set (10.06.2017) and spatially relative to the reference point (Table S1, column 7). Based on ground temperature data and onset of frost heave on InSAR time series, we estimated an average initiation date of ground freezing (02.10.2017) used to map separately the ground displacements of the thawing period (102 days between June and October 2017) and the start of the freezing period (60 days between October and December 2017). In practice, the onset of frost heave varies spatially, but a unique date was chosen to present the results in a homogenous way.

### 3.3. Comparing 2D InSAR to geomorphology

The TSX 2D InSAR displacement rates were compared to a detailed geomorphological map available for this area (Härtel and Christiansen, 2014), which is the most updated version of a geomorphological and quaternary geological map in Adventdalen (modified from Tolgensbakk et al., 2001). Geomorphological units were extracted, simplified and partly renamed from the existing maps to allow for direct comparison with InSAR (Fig. 2). Punctual (e.g. individual boulders or forms) and linear (e.g. gullies or ridges) forms were discarded. Initially separated units ‘Weathered material, autochthonous’ and ‘Weathered material, allochthonous’ were merged into ‘Regolith’, just as ‘Fluvial material, recent’ and ‘Fluvial material, pre-recent’ and ‘Braided-river plain’ were merged into ‘Fluvial sediment’. The classes ‘Sea and lake’, ‘Foreshore flat’ and ‘Glacier’ are not taken into account (unselected, dark grey in Fig. 2) as InSAR provides no relevant information on these surfaces. The units ‘Alluvial fans’ and ‘Talus cones’ are not differentiated and are displayed according to their sediment type ‘Alluvial sediment, recent’, ‘Alluvial sediment, pre-recent’ or ‘Colluvium’ respectively. For statistical reasons (too few comparable pixels), the units ‘Organic material’ and ‘Pingo’ were not taken into account (unselected, dark grey in Fig. 2). Solifluction is defined as surficial material in the original maps despite that it is a landform, not a material type. It is called ‘Solifluction’ in the simplified map. The final simplified map is composed of 14 units including 11 corresponding to natural sediments and bedrock, two corresponding to landforms (‘Solifluction’ and ‘Rock glacier and protalus rampart’) and one corresponding to artificial surficial material (‘Anthropogenic material’).

The 14 units have large differences in spatial extent, from approximately 1 km<sup>2</sup> of ‘Rock glacier and protalus rampart’ to approximately 158 km<sup>2</sup> of ‘Regolith’. In addition, the coverage of InSAR maps is not continuous due to low coherence and layover/shadow areas that have been masked out. This causes high variability in the distribution of InSAR pixel numbers corresponding to the different geomorphological units. For further comparison, we randomly selected 3000 2D InSAR pixels per unit following the methodology described by Eckerstorfer et al. (2018). The location of the selected pixels is shown in Fig. S5 (Supplementary material). For each unit, the median, first and third

quartiles, inter-quartile range, maximal/minimal values were calculated. Significance tests (F-test of Fisher and Welch two sample *t*-tests) were performed to compare the variance and mean of each geomorphological unit and estimate if they significantly differ. The pixel frequency per class of 10 mm displacement rate was analysed for the vertical and horizontal components separately and scatter plots combining the two components were created to visualise the 2D behaviours of each single pixel.

### 3.4. Comparing InSAR time series to ground temperature

The S1 InSAR time series was compared to ground temperature data from two boreholes in the central part of the study area: Adventdalen (ADV) and Endalen (END) (Figs. 1 and 2). ADV is located north of the river flowing in Adventdalen (Adventelva) in a flat area covered by eolian sediment. END is located on the north-western slope of Endalen affected by solifluction. Information about the boreholes is summarized in Table 2. The analysis consists of a comparison of timing and trends between InSAR and temperature time series. Due to the intrinsic differences of physical measures and data properties (unit, temporal sampling, spatial resolution, etc.), the analysis is based on a visual interpretation of the respective trends.

## 4. Results

### 4.1. InSAR results

The results of the multi-year InSAR stacking for each SAR dataset provide a spatial overview of the average LOS displacement rates based on three (S1) to nine (TSX) thawing seasons (Fig. 3). Fig. 4 shows detailed results for three smaller areas. For comparison, we focus on TSX and S1 results both in ascending geometry, expressed in average displacements (mm) along their respective LOS during the 4-month thawing periods (summer). The results from TSX descending stacking are available in the Supplementary material (Fig. S6). Positive values show an increase of the sensor-to-ground distance (displacements away from the radar), whereas negative values show a decrease of the sensor-to-ground distance (displacements towards the radar). As indicated in Table 1 and with black arrows in Figs. 3 and 4, the LOS is quite similar for both datasets.

At a regional scale, the main patterns on both maps are similar, both in terms of magnitude of displacements and spatial variations. Thanks to its C-band sensor and 6-day revisit time, S1 provides a better spatial coverage in fast moving and moist ground in Adventdalen due to higher coherence. The sediments on the terraces surrounding the Adventdalen braided river are largely settling due to the phase change from ice to water in the active layer. Maximal average values are up to ca 230 mm/summer (Fig. 4, area 3), but the results highlight spatial variations partly following the delineation of geomorphological units. In the adjacent valley bottoms (Longyeardalen, Endalen, Todalen) and in low flat areas such as in the north-western part of the study area (Svalbard airport area), displacement rates are generally lower. On west-facing

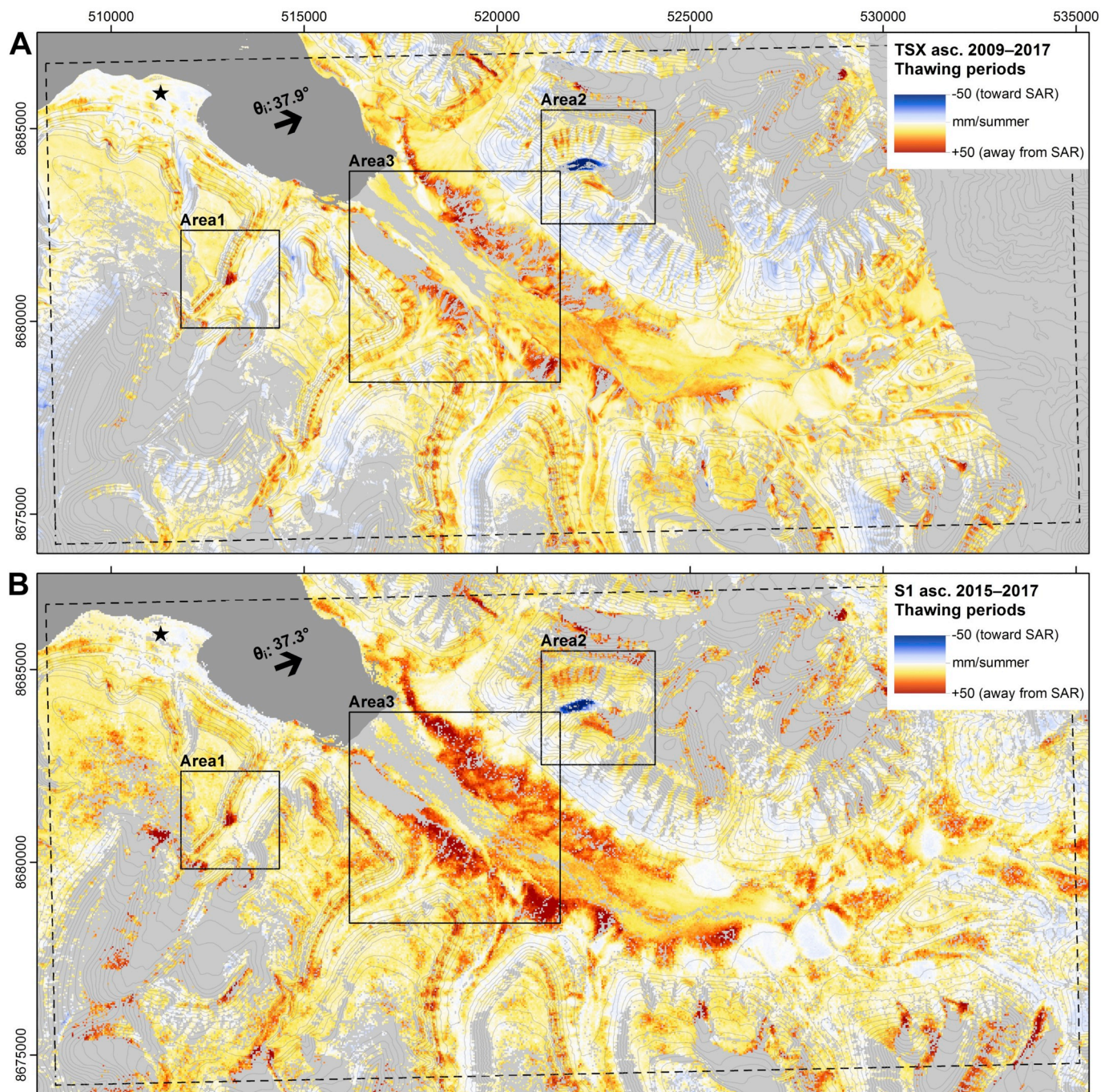


**Fig. 3.** Multi-year InSAR stacking LOS displacement rates during the 4-month thawing periods (June to September). A. Results from TerraSAR-X stacking, StripMap Mode, ascending geometry. B. Results from Sentinel-1 stacking, Interferometric Swath Mode, ascending geometry. Note that the observation period is not similar (2009–2017 for TerraSAR-X, 2015–2017 for Sentinel-1) and that the colour scale is saturated for visualisation. Black arrows: LOS orientations (label  $\theta_i$ ; incidence angles). Black squares: areas shown in Fig. 4. Dashed black rectangle: extent of geomorphological map shown in Fig. 2. Black star: reference point (Svalbard airport building). Background: land/sea masks and 50 m contour lines (Norwegian Polar Institute, 2014b).

slopes, little displacement is detected due to the unfavourable orientation compared to the ascending LOS. Some areas show a decrease of sensor-to-ground distance highlighting a horizontal component towards the radar. The most obvious example is located in Ugledalen where a debris-covered glacier is moving towards the radar with maximal average values up to ca 370 mm/summer (Fig. 4, area 2). On east-facing slopes, more active areas are mapped due to the more favourable slope orientation compared to the LOS. These displacements away from the radar can be associated with rock instabilities on rock noses, regolith and colluvium in upper parts of the slopes, and creep

processes on solifluction sheets, rock glaciers and protalus ramparts in the middle and lower parts of the slopes (Fig. 4, areas 1–3). The most obvious example is located in Longyeardalen and corresponds to a rock glacier moving towards east (away from the radar) with maximal average values up to ca 320 mm/summer (Fig. 4, area 1). Areas without any InSAR result (grey in Figs. 3 and 4) are either affected by significant changes in surface properties due to e.g. moisture, snow or fast displacements (coherence under chosen thresholds), or by layover or shadow (see Section 3.2). The differences between TSX and S1 results are related to intrinsic differences between the sensors and datasets

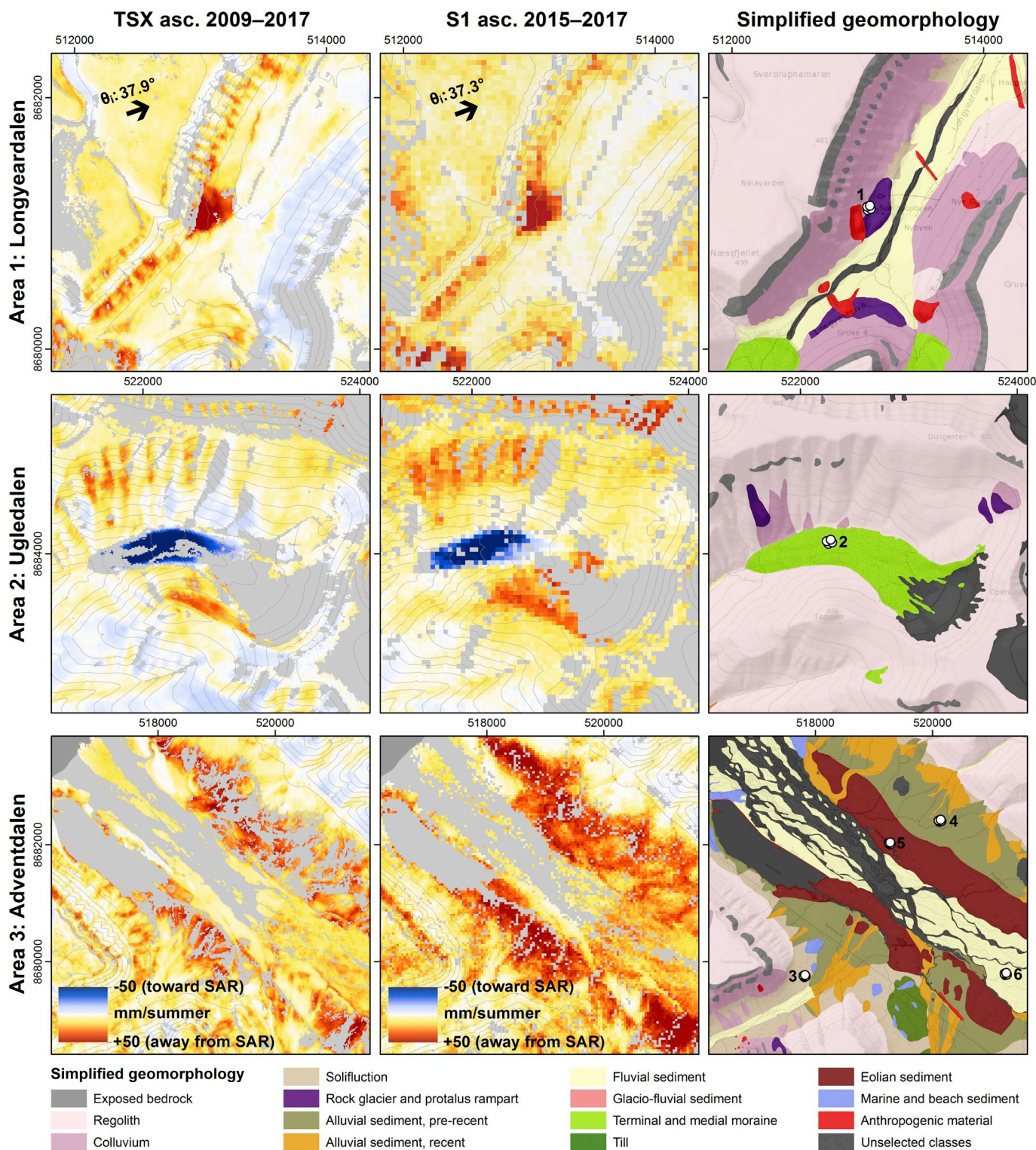
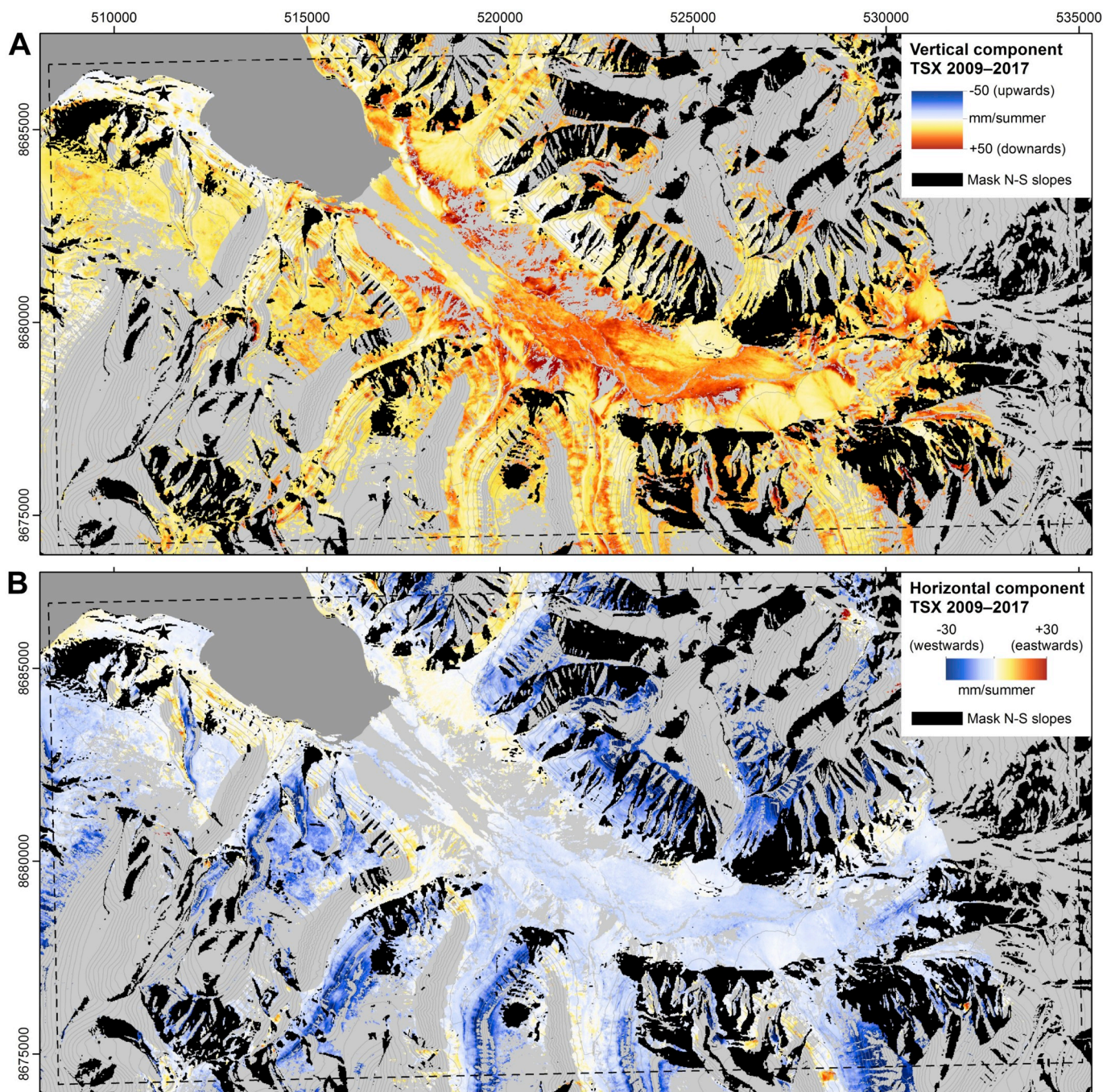


Fig. 4. Comparison of TerraSAR-X and Sentinel-1 ascending multi-year stacking LOS displacement rates during the 4-month thawing periods (June to September 2009–2017 for TerraSAR-X, 2015–2017 for Sentinel-1) with the simplified geomorphological map in areas of measured high displacement rates. Locations of the areas are shown in Figs. 2 and 3. In first and second columns: black arrows show the LOS orientations (label  $\theta_i$ ; incidence angles). In third column: circled white dots show the location of time series presented in Fig. 7.

(observation periods, temporal and spatial resolutions, sensor wavelengths, LOS, etc.) and are further discussed in Section 5.1.

Fig. 5 shows the results of the vertical (upwards-downwards, Fig. 5, A) and horizontal (eastwards-westwards, Fig. 5, B) decomposition based on the combination of TSX ascending and descending InSAR stacking. The map of the magnitude of 2D vectors is available in the

Supplementary material (Fig. S7). The steep incidence angle of the descending geometry (Table 1) induces extensive layover on slopes facing the radar, which unfortunately leads to a reduced common 2D InSAR area on east-facing slopes. As explained in Section 3.2, N-S slopes affected by rate underestimation are masked out (black mask, Fig. 5). The results show settlement caused by thaw subsidence at variable rate



**Fig. 5.** Vertical/horizontal decomposition based on combination of TerraSAR-X ascending and descending multi-year stacking displacement rates during the 4-month thawing periods (June to September 2009–2017). A. Vertical component. B. Horizontal component. Black star: reference point (Svalbard airport building). The magnitude of 2D vectors is shown in Fig. S7 (Supplementary material). Background: land/sea masks and 50 m contour lines (Norwegian Polar Institute, 2014b).

over flat areas and the combination of vertical and horizontal displacement components on slopes. As expected, flat areas in valley bottoms, on mountain plateaus and on the lowland raised marine deposits have a low horizontal component of displacement.

The S1 SBAS time series retrieved between June and December 2017 highlights the change from subsidence to heave in beginning of October in most of the flat areas (Fig. 6). Between June and beginning of October, the sensor-to-ground distance generally increased on flat areas (Fig. 6, A) due to thaw subsidence, while it generally decreased from September to December due to frost heave (Fig. 6, B). On the slopes, the time series does not necessarily follow the same subsidence and heave pattern due to gravity-driven processes and their impact on

the detected displacements with respect to the LOS. Lower subsidence and heave amplitude can also be explained by less frost-susceptible coarse material and lower water content as it drains downhill and accumulates in valley bottoms. It should be noted that even after having masked out low coherence pixels, the quality of the results on the top of the plateaus is variable. Especially in the south-western part of the area, large variations of values at short intervals in space and time indicate that pixels may be affected by noise most likely related to changes in surface properties due to snow and moisture. This is further discussed in Section 5.1.

S1 2017 time series on selected sediments and landforms (Fig. 7) shows clear seasonal variability in the movement pattern. The

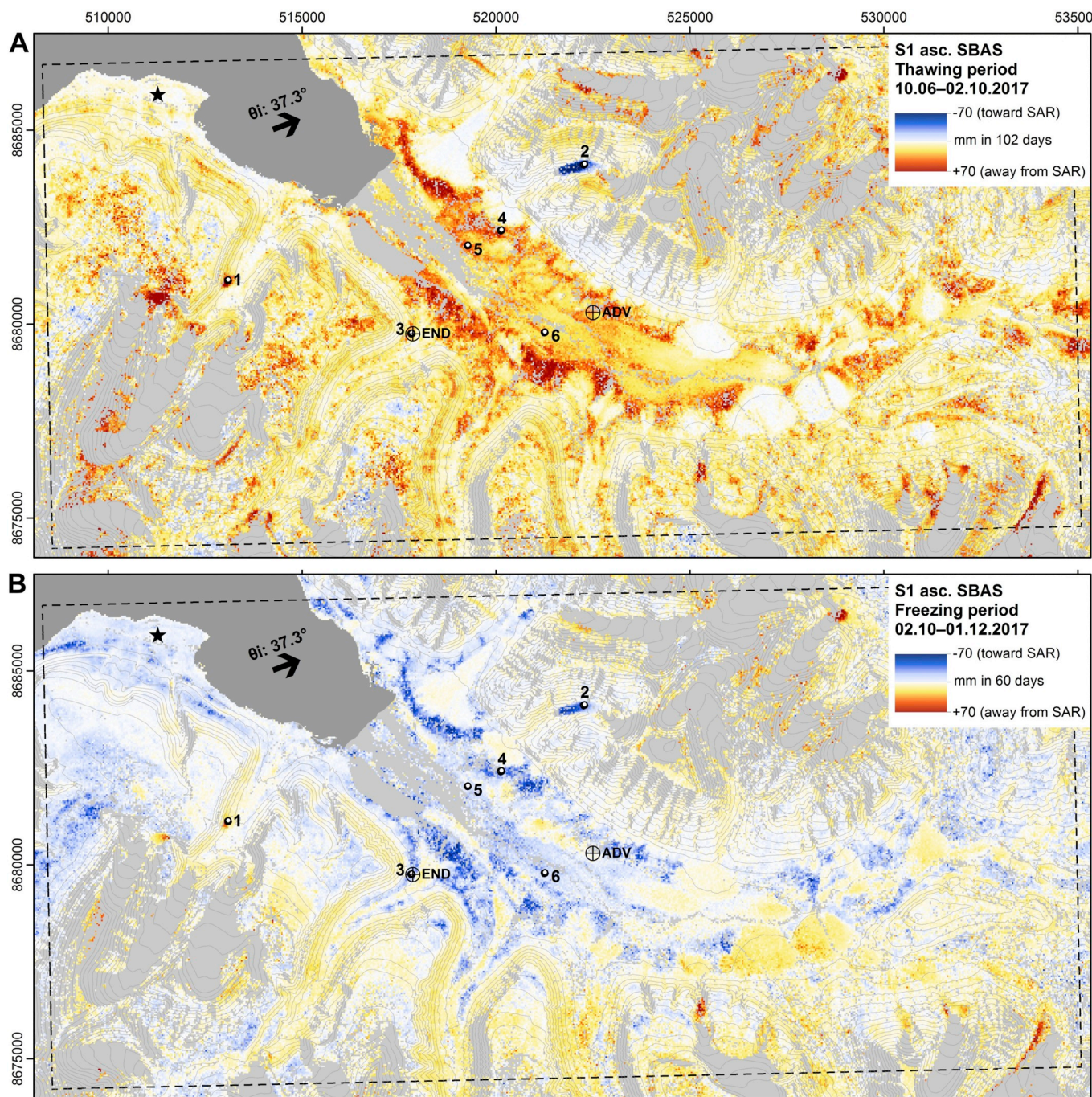


**Fig. 6.** Total Sentinel-1 SBAS LOS displacements during the thawing period (June to October) and the start of the freezing period (October to December) 2017. A. 10.06 to 02.10.2017 total LOS displacements highlighting thaw subsidence, especially in the lowlands. B. 02.10 to 01.12.2017 total LOS displacements highlighting frost heave, especially in the lowlands. Black arrows: LOS orientations (label  $\theta_i$ : incidence angles). Circled white dots: location of time series presented in Fig. 7. Black crossed circles: location of Endalen (END) and Adventdalen (ADV) boreholes. Black star: reference point (Svalbard airport building). Background: land/sea masks and 50 m contour lines (Norwegian Polar Institute, 2014b).

comparison of four neighbouring pixels shows the consistency of the displacement patterns and the magnitude of the spatial variability for an 80 m × 80 m window. Located on slopes with 10–14° angles, the rock glacier and the debris-covered glacier (Fig. 7A, graphs 1 and 2) are mainly controlled by gravity-driven processes. The velocity varied during the measurement period (Fig. 7B, lines 1 and 2) but no clear trend related to the active layer thawing and freezing can be highlighted due to the superimposed downslope creeping process. LOS displacements reached 80 to 120 mm in 6 months (away from the radar for the rock glacier in Longyeardalen due to its eastward orientation,

towards the radar for the debris-covered glacier due to its westward orientation). For the solifluction sheet (Fig. 7A, graph 3), creep is also expected due to the 8.8° slope angle at this location, but the subsidence and heave related to the active layer thawing and freezing are large enough to dominate the measured displacement pattern. Velocity was at its maximum during the initial thawing period from mid-June to early July (Fig. 7B, line 3). It then decreased and stayed relatively stable through the summer before it increased again between the end of September and mid-October. Graphs 4–6 (Fig. 7A) show examples of different sediments in the bottom of Adventdalen. Due to the nearly flat

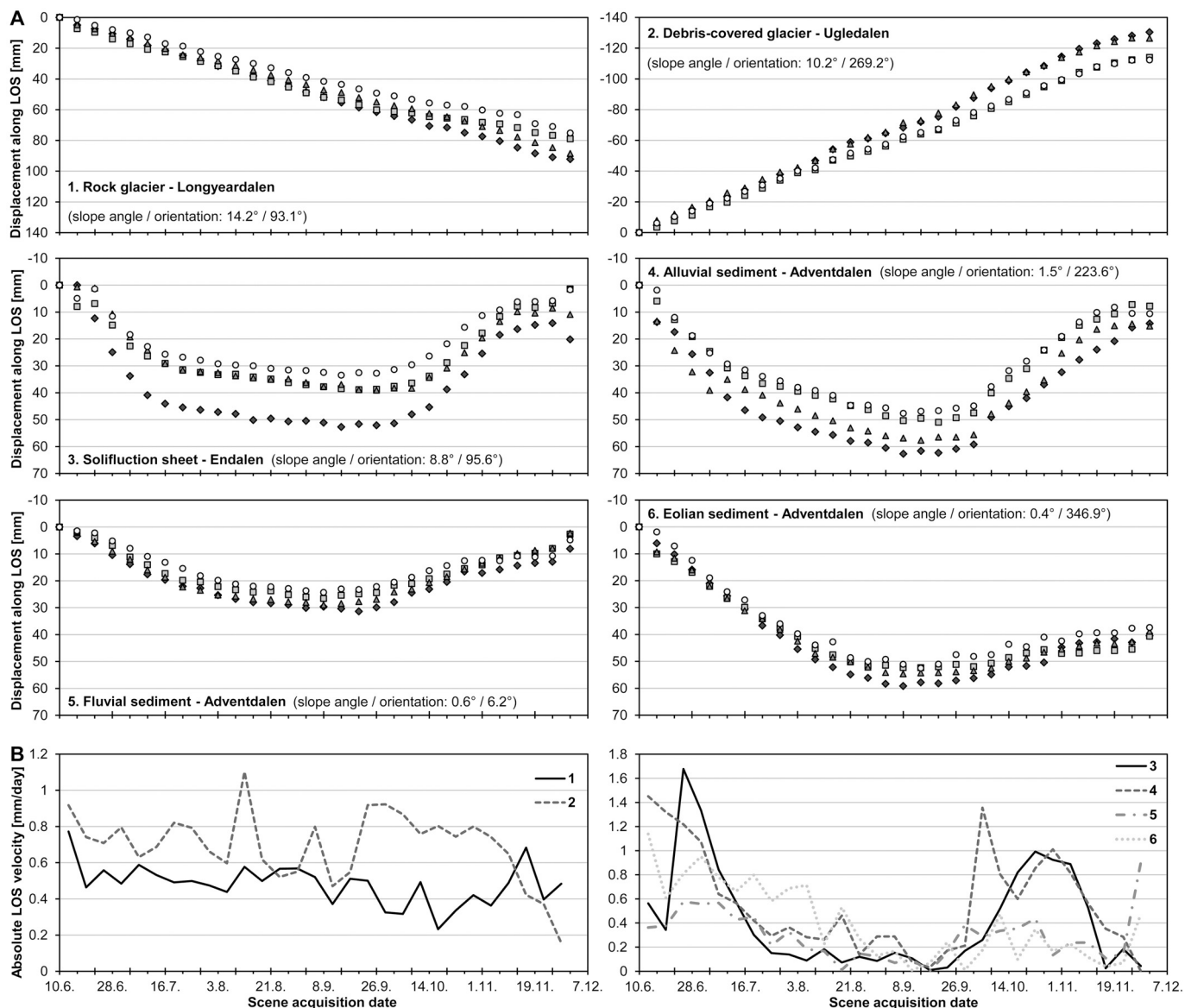


**Fig. 7.** A. Sentinel-1 SBAS June to December 2017 LOS displacement time series at six locations with different sediments and landforms. The four different symbols show the time series for four neighbouring pixels, highlighting the magnitude of the spatial variability for an 80 m × 80 m window. Time series 1. and 3. are located on east-facing slopes, 2. on west-facing slope, 3–6 on flat Adventdalen valley bottom. Locations of the time series are represented by the white dots in Figs. 4 and 6. B. Absolute LOS velocity between consecutive acquisitions based on the average of the four neighbouring pixels at the six selected locations. 1. and 2. are landforms mainly controlled by gravity-driven processes and thus dominated by a downslope pattern, 3–6 are landforms mainly controlled by the active layer dynamics and thus dominated by a subsidence/heave pattern. Note that the range of values on vertical axes varies for the different graphs.

topography (slope angles: 0.4–1.5°), the measurements are clearly dominated by thaw subsidence and frost heave at different magnitudes. At its maximum, the detected subsidence reached 60 mm in alluvial (Fig. 7A, graph 4) and eolian sediments (Fig. 7A, graph 6), but only 30 mm in fluvial sediment (Fig. 7A, graph 5). For all subsidence/heave-dominated time series (Fig. 7B, lines 3–6), velocity was high in June and early July and decreased later in the summer. The ground surface was generally stable in September, and the heave started quickly at the beginning of October before slowing down in mid-November. Even if the different landforms highlight a similar trend, the magnitude varies significantly depending on the location. The identification of specific displacement rates for different geomorphological units highlights the need for more detailed investigation of the InSAR spatial variability, presented in Section 4.2. Further interpretations of the temporal variations are presented in Section 4.3.

#### 4.2. Comparing 2D InSAR to geomorphology

Statistics of the 2D InSAR average displacements during the thawing seasons 2009–2017 are analysed for each of the 14 selected geomorphological units (see Section 3.3). Three main observations show that there is a relationship between the magnitude of the 2D InSAR displacements during the thawing periods and the geomorphological units (Fig. 8): (1) the median value per unit varies between 4.5 mm/summer and 29.5 mm/summer, with minimum values in ‘Marine and beach sediment’ and ‘Anthropogenic material’ and a maximum value in ‘Eolian sediment’; (2) ‘Rock glacier and protalus rampart’, ‘Terminal and medial moraine’, and ‘Eolian sediment’ have a median > 5 mm/summer over the median of all pixels, while ‘Marine and beach sediment’ and ‘Anthropogenic material’ have a median > 5 mm/summer below; (3) the interquartile range (IQR) varies between certain units: ‘Terminal and medial moraine’ and ‘Eolian sediment’ have an IQR at

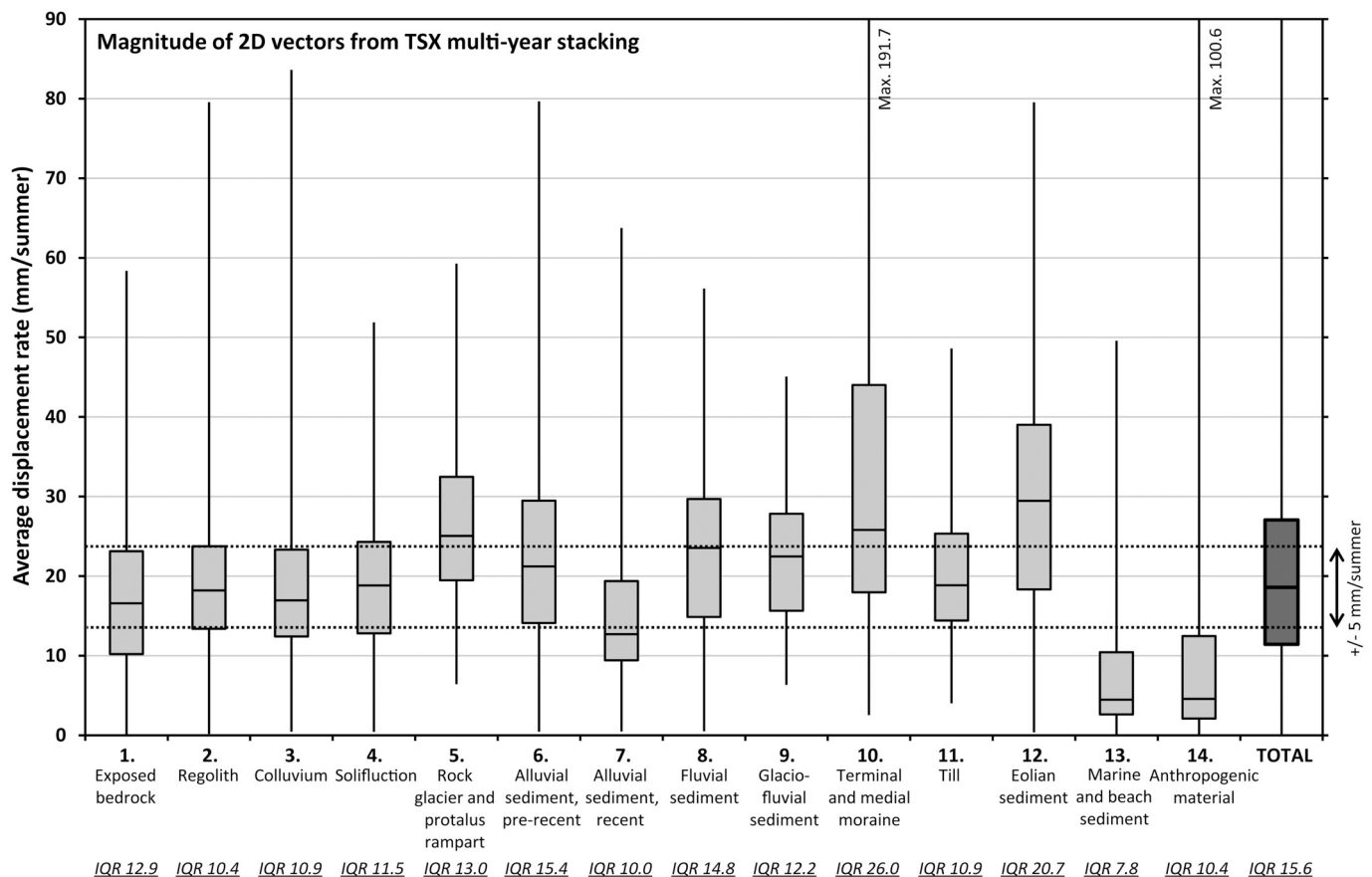


Fig. 8. Magnitude of 2D vectors from TerraSAR-X multi-year stacking for each geomorphological unit during the 4-month thawing periods (June–September 2009–2017). For scaling and visualisation purposes, the maximum displacement rates of ‘Terminal and medial moraine’ and ‘Anthropogenic material’ are higher than the upper limit shown. The last box on the right corresponds to statistics of all 42,000 pixels together. The dotted line shows the  $\pm 5$  mm/summer limits over/under the median of all pixels. IQR values are the interquartile range for each unit. Note that the bedrock is exposed mainly in rock noses in the upper steep part of the slopes. As some of these areas are unstable, high displacement rates are expected.

least 5 mm/summer higher than for the overall pixel average. ‘Regolith’, ‘Alluvial sediment, recent’, ‘Marine and beach sediment’ and ‘Anthropogenic material’ have an IQR at least 5 mm/summer lower.

Results from significance tests show that the hypothesis of no difference between the means of all pairs of geomorphological units can be rejected in most cases, confirming that the displacement rate differs significantly depending on the geomorphology (Fig. S8 in Supplementary material). Despite these differences, there are large overlaps in the 2D value ranges for most of the units and statistical similarities are found between some of them. *P*-values are over 0.05 between ‘Regolith’ and ‘Colluvium’, ‘Alluvial sediment, pre-recent’ and ‘Fluvial sediment’, and ‘Glacio-fluvial sediment’ and ‘Fluvial sediment’. *P*-values are over 0.01 between ‘Regolith’ and ‘Solifluction’, ‘Colluvium’ and ‘Solifluction’, and ‘Alluvial sediment, pre-recent’ and ‘Glacio-fluvial sediment’ (Fig. S8).

The vertical and horizontal components provide more information (boxplots in Figs. S9–S10 in Supplementary material), and can also be analysed by studying the pixel frequency per class of 10 mm/summer displacement rates (Fig. 9) and magnitude of 2D vectors in Fig. S11 of the Supplementary material). Four main observations highlight the value of the 2D InSAR decomposition: (1) for low values of displacement rates (0 to +20 mm/summer for the vertical component, –10 to +10 mm/summer for the horizontal), all geomorphological units are represented with a frequency between 3 and 15% of the pixels; (2) for higher positive rates for the vertical component (over 50 mm/summer downwards), ‘Alluvial sediment, pre-recent’, ‘Terminal and medial moraine’ and ‘Eolian sediment’ represent over 80% of the pixels; (3) for higher absolute displacement rates for the horizontal component (over

30 mm/summer), ‘Rock glacier and protalus rampart’, ‘Terminal and medial moraine’ and ‘Anthropogenic material’ represent over 60% of the pixels; (4) vertically, the presence of low negative rates (upwards, min: –6.5 mm/summer) mainly for ‘Marine and beach sediment’ and ‘Anthropogenic material’ can be attributed to a slight shift due to subsidence at the reference point (further discussed in Section 5.1).

The limitation of this histogram analysis is that it artificially separates vertical and horizontal components that can, if analysed in combination, provide further information about the orientation of the displacements. To visualise the 2D behaviour of each single pixel, results are presented as scatter plots. Six of the most widespread geomorphological units are shown (Fig. 10). The remaining results are available in the Supplementary material (Fig. S12). The variability of the 2D InSAR results highlights the control of the topography. On slopes, gravity-driven processes induce downslope movement combining vertical and horizontal components. ‘Solifluction’ (Fig. 10, plot A) is affected both by horizontal (up to 32 mm/summer) and vertical displacements (up to 50 mm/summer). The vertical component is overall higher than horizontal component, which fits with field measurements (Harris et al., 2011). ‘Rock glacier and protalus rampart’ (Fig. 10, plot B) has a higher horizontal component (up to 50 mm/summer, mainly westwards due to the overrepresentation of west-facing slopes) combined with high vertical components (up to 53 mm/summer). In the lowlands, the horizontal component is negligible due to low slope angles. ‘Fluvial sediment’ (Fig. 10, plot C) and ‘Eolian sediment’ (Fig. 10, plot D) are mainly distributed along the vertical axis with high subsidence rates up to 40 and 60 mm/summer respectively, but characteristically without much horizontal movement. Measured low horizontal rates can, however, be

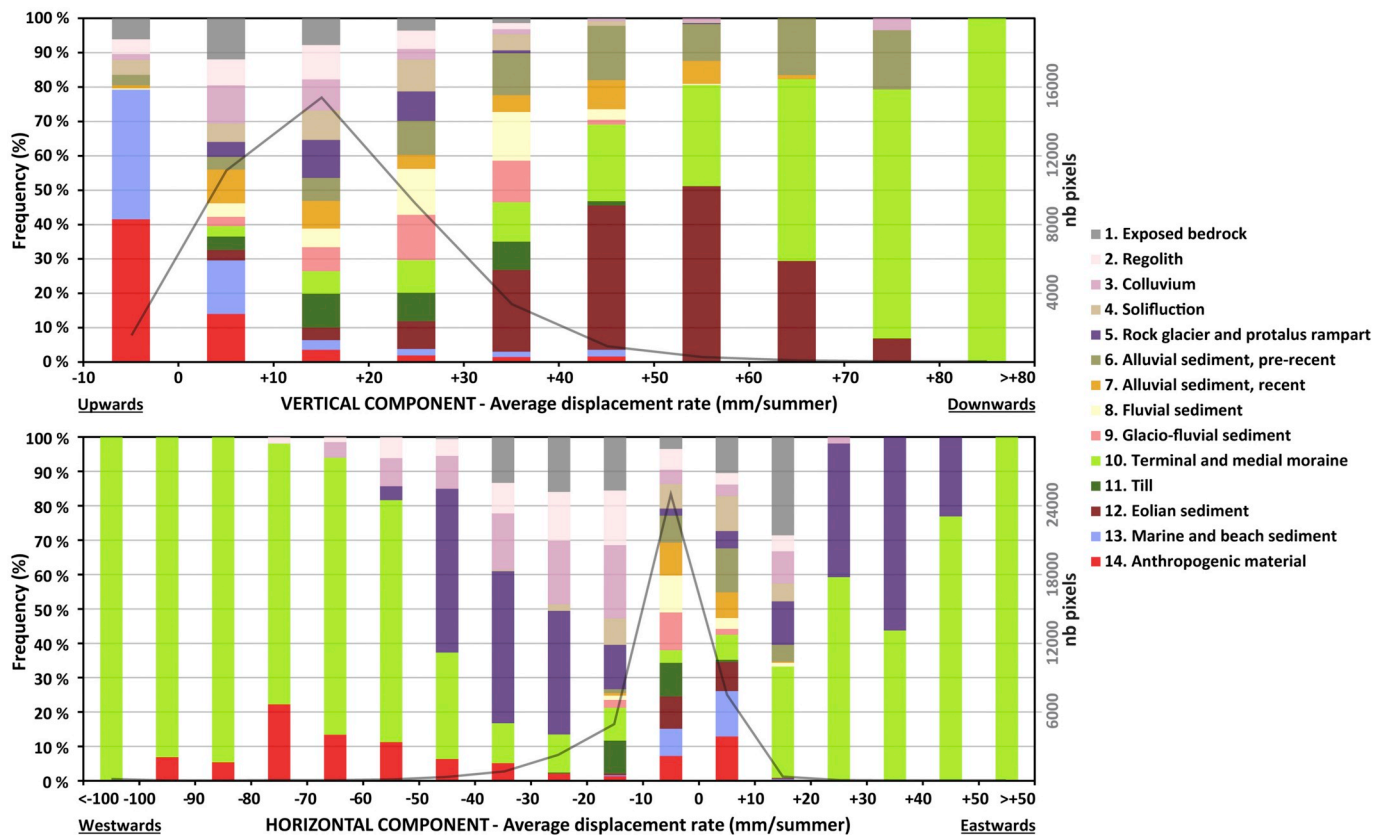


Fig. 9. Pixel frequency per class of 10 mm/summer displacement rates based on 2D InSAR from TerraSAR-X multi-year stacking during the 4-month thawing periods (June–September 2009–2017). Upper: Vertical component. Lower: Horizontal component. The geomorphological units and attributed colours are similar to those presented in Fig. 2. The grey curves indicate the number of pixels per class of 10 mm/summer displacement rates showing that 100% at high displacement rates correspond to fewer pixels than low rates. The shift of the horizontal displacements towards the west is due to the overrepresentation of west-facing slopes. Magnitude of 2D vectors is shown in Fig. S11 (Supplementary material).

due to creep on low-angled slopes and the slight shift towards negative values is again due to an overrepresentation of west-facing slopes. The difference of magnitude between ‘Fluvial sediment’ and ‘Eolian sediment’ can be related to the ground porosity, the frost-susceptibility of the material, as well as the water content and availability. The sand-gravel portion in fluvial sediment constrains both the porosity and frost-susceptibility. Fine-grained eolian sediment is more favourable to cryosuction, which controls the supply of water at the freezing front and thus enable ice segregation and ice lens formation (French, 2007; Smith, 1985), lifting the ground surface during freezing. ‘Terminal and medial moraine’ (Fig. 10, plot E) shows a core of values with rather low rates, but a large number of outliers with extreme rates in both components (up to 187 mm/summer horizontally and 102 mm/summer vertically). These areas are highly dynamic as they are located at the front or on the edges of retreating land-terminating glaciers. InSAR documents several potential processes going on in these landforms: mass-wasting, thawing of ice-cores, or creep of glaciers that are debris-covered but have been mapped as moraines. For ‘Anthropogenic material’ (Fig. 10, plot F), two different patterns are highlighted: vertical displacements at low rates over infrastructure in lowlands (mainly below 20 mm/summer), and higher rates including a large horizontal component corresponding to mining deposits located on valley slopes. This indicates that some mining piles are moving downslope. Composed of coarse material and located on steep slopes ( $> 30^\circ$ ), the behaviour of these artificial landforms can be compared to natural permafrost creep process.

#### 4.3. Comparing InSAR time series to ground temperatures

The S1 InSAR time series between June and December 2017 highlights clear seasonal variations (Fig. 7) that can be compared to in situ temperature measurements between the ground surface and 2 m depth at the Adventdalen (ADV) and Endalen (END) boreholes (see Section 3.4).

Due to loss of coherence on snow and wet surfaces, the InSAR results potentially miss the start of the thaw subsidence and more importantly part of the frost heave when the ground gets snow-covered. Thus, the results are not able to provide the absolute magnitude of the subsidence and heave through a one-year cycle. In addition, InSAR time series correspond to displacements along LOS, regardless of the slope angle and orientation. Consequently, we focus on the timing and the relative changes of trends rather than on the absolute displacement values. The analysis provides information about the temporal variations of movement, compared to the field-measured ground temperatures.

The time series documents the summer thawing, the autumn freezing and the start of the winter cooling, as described in Zhao et al., 2000. In Fig. 11, the match between the ground temperature variations and InSAR displacement is obvious during four time periods: (1) Subsidence starts at – or rapidly after – the beginning of the ground thawing, when SAR scenes become snow-free and exploitable for InSAR analysis. The first acquisitions can, however, be affected by noise and phase ambiguities attributed to moisture or too fast movements (between 10.06.2017 and 22.06.2017 at END). Fast subsidence due to the quick thawing of the top active layer is measured during approx. two months. (2) From beginning of August, a second period is characterized by slower subsidence, when surface and shallow temperature starts

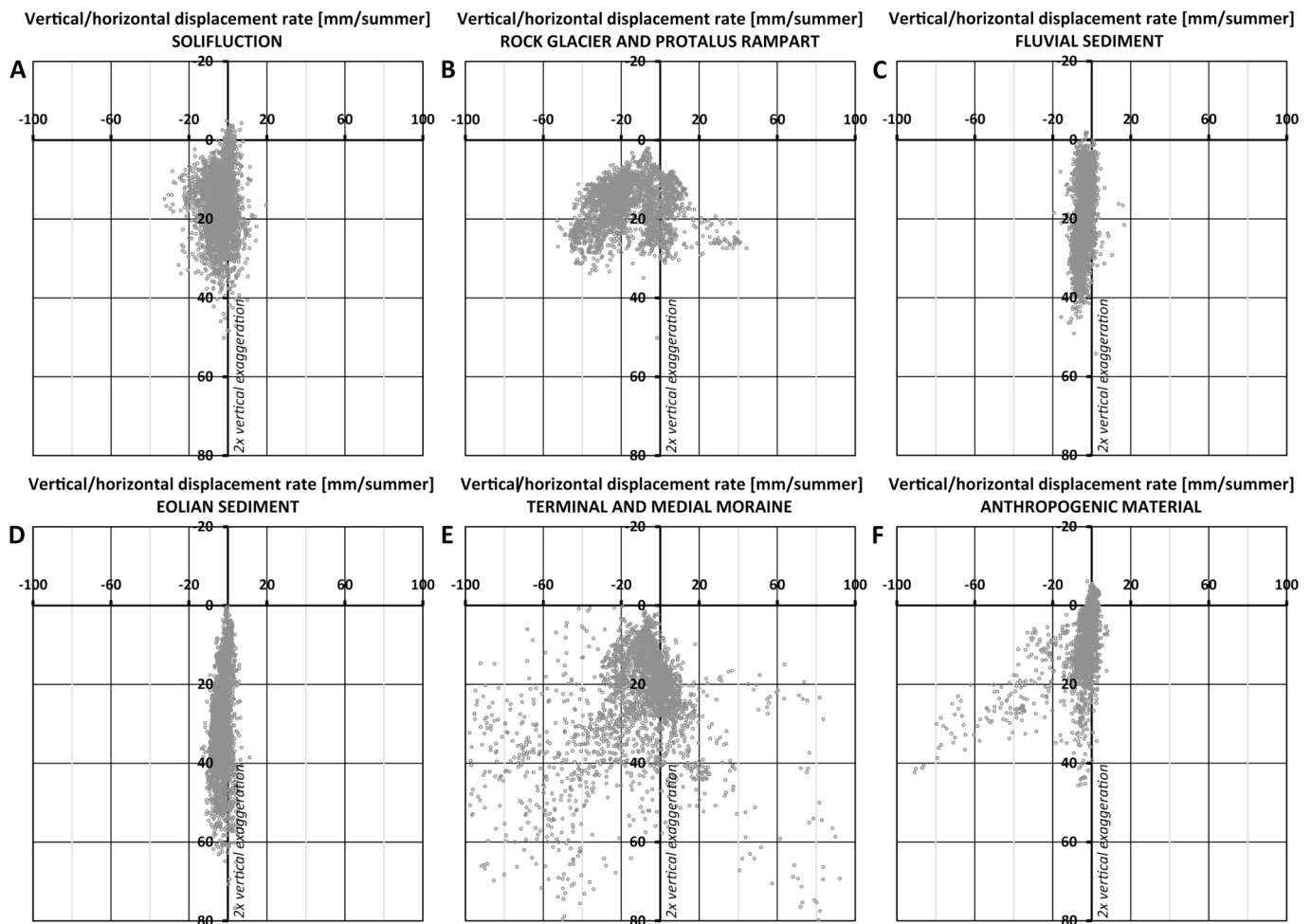


**Fig. 10.** Scatter plots showing the horizontal (x-axis) and vertical (y-axis) displacement rates of the 3000 randomly selected pixels for six geomorphological units based on 2D InSAR from TerraSAR-X multi-year stacking during the 4-month thawing periods (June–September 2009–2017). Note that E has the same scale as A–F for comparison, so pixels with large rates are not visible. In Fig. S12 (K in Supplementary material), the limits of the axis have been doubled to see all values.

decreasing but the deeper active layer slowly still develops. The second period lasts approx. two months. (3) Short transition from subsidence to heave recorded by InSAR matches the initiation of the active layer freeze-back period, which occurs between the end of September and the beginning of October at both sites. (4) Even short-term temperature fluctuations appear to have a halting impact on ground displacements; for example in beginning of November at ADV and more clearly in the middle of November at END, the heave slows down before speeding up again, corresponding to a short-term ground surface warming.

The seasonal evolution of the ground surface dynamics resolved into subsidence and heave correspond to patterns documented in previous studies also based on in-situ and remote sensing measurements (Daout et al., 2017; Harris et al., 2011; Smith, 1985; Strozzi et al., 2018). Modelling the variations of the thaw/freezing depths based on the Stefan function (Nelson et al., 1997) and proportionally relating the depth of the thawing/freezing front to displacements caused by the phase change of ground water (Hu et al., 2018) have shown that the cyclic elevation changes are primarily controlled by the thermal response of the active layer to atmospheric forcing. In Adventdalen and Endalen, we show that the high temporal resolution of S1-based InSAR results can be used as an indirect tool for monitoring active layer temperature changes in permafrost environments. This is further discussed in Section 5.3.

## 5. Discussion

### 5.1. Multi-sensor and multi-geometry complementarity

Our results highlight the complementarity of multi-sensor and multi-geometry InSAR. At the regional scale, the patterns detected on stacking results based on ascending geometries from S1 and TSX sensors are consistent overall (Fig. 3). However, several differences related to the intrinsic properties of the two sensors and datasets highlight the value of taking benefit of their respective advantages. The C-band wavelength and 6-days revisit time of S1 provide less decorrelation and better coherence on wet and fast moving surfaces, compared to X-band and 11-days revisit time of TSX (e.g. valley bottom, Fig. 4, area 3), as also discussed by Antonova et al. (2018) and Strozzi et al. (2018). Comparison between S1 SBAS time series and ground temperatures shows the value of the S1 short revisit time to document seasonal patterns. The scene coverage of 250 km (swath wide) and the open data policy of the Copernicus Programme are valuable for upscaling the investigation of periglacial landscapes and make possible the development of operational monitoring services. On the other hand, the 15 m spatial resolution of TSX after multilooking (compared to 40 m for S1) allows for more detailed investigation of small-scale landforms (e.g. rock glaciers and debris-covered glaciers, Fig. 4, areas 1 and 2). Comparison between TSX 2D InSAR results and geomorphology shows the value of the availability of two geometries allowing for 2D InSAR decomposition. Until the end of 2017, no descending image was available

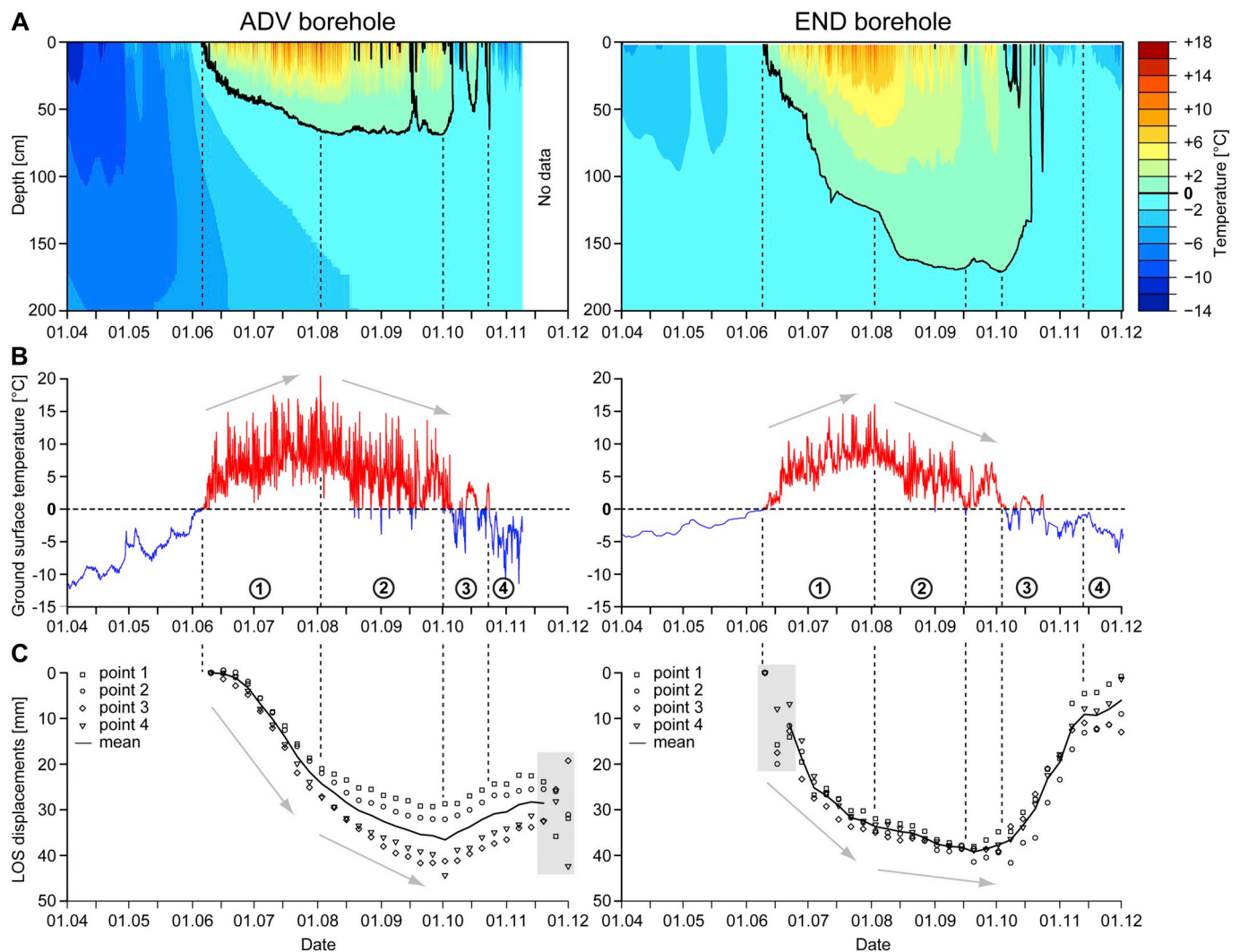


**Fig. 11.** 2017 ground temperature and Sentinel-1 SBAS displacement time series during summer thawing, autumn freezing and start of winter cooling at borehole locations. Left: Adventdalen (ADV) borehole. Right: Endalen (END) borehole. A. Temperature from the ground surface down to 200 cm depth. B. Ground surface temperature. C. InSAR displacements at the four neighbouring pixels closest to the two boreholes. The vertical dashed lines and circled numbers correspond to the four identified matching time periods. Grey areas: acquisitions affected by noise. Information about the two boreholes is summarized in Table 2 and their locations are shown Figs. 1, 2 and 6.

for S1 Interferometric Wide Swath mode in the study area. Other differences may be related to the different observation periods, spatial and temporal resolutions and LOS.

Error sources and uncertainties in InSAR results have to be taken into account. Large scale unwrapping problems have been mitigated by manually discarding affected interferograms. However, some local unwrapping errors can be expected, especially on small areas isolated by non-coherent ones (e.g. south-western part of the study area, Fig. 3). The mitigation of the tropospheric effect is performed by stacking (averaging) of interferograms or using a network-based approach for SBAS. The standard deviation of the retrieved velocity depends on the number of interferograms (71–99) and the maximum temporal baseline (22–24 days) used for the processing. Using Eq. 11 from Emardson et al. (2003) and assuming a standard deviation of 5 mm per interferogram due to the atmosphere, the standard deviation of the stacking results in Adventdalen is estimated to 2.5–3.5 mm/summer. Other unwanted phase change components related to changes of surface properties (vegetation, snow, moisture) can also have an impact on the accuracy of the results, but are unfortunately difficult to assess quantitatively. Seasonal change of ground moisture is most likely the main error source in this study. It induces differential propagation of the electromagnetic

wave into the ground, leading to a biased detection of sensor-to-ground change of distance (De Zan et al., 2014). The bias of the phase measurements due to ground moisture variability increases with the radar wavelength and can reach 10–20% of the wavelength (Zwieback et al., 2017). Thus, S1 results are more susceptible to this effect than TSX. The bias typically corresponds to an overestimation of the subsidence during the thawing season (due to a decrease of the wave velocity as the ground gets moister). Though the magnitude of the detected displacements, the consistency of the patterns from both sensors (Fig. 3) and the clear inversion from subsidence to heave fitting the timing of ground thawing and freezing (Figs. 7, 11) tend to indicate that our results are overall robust, this issue would definitely benefit from further research. As discussed by Zwieback et al. (2017), the sensitivity of InSAR to ground moisture can in addition become valuable if this phase contribution can be isolated. Finally, due to the highly dynamic Svalbard environment, finding a stable reference point is not easy. Some upward values over flat areas on the stacking results based on the thawing periods may indicate an upward shift of the mean velocity (< 7 mm/summer) due to slight subsidence at the pixel chosen as reference point.

## 5.2. InSAR contribution for geomorphological investigation

Our results highlight that vertical and horizontal displacement patterns in and around Adventdalen vary for different geomorphological units. On slopes, InSAR results provide good delineation of creeping landforms (e.g. rock glaciers, debris-covered glaciers, solifluction sheets). The landforms combine vertical and horizontal components of displacement at variable rates controlled by the involved processes. Over low-relief areas, vertical displacements naturally dominate and the seasonal amplitude is particularly large in fine-grained frost-susceptible materials (e.g. eolian sediment) and areas assumed to have good water availability (e.g. outer part of alluvial fans). This confirms the findings of [Daout et al. \(2017\)](#) who highlighted that seasonal ground displacements are largely controlled by ground properties and water content in the sedimentary basins of the Tibet Plateau. For example, in Adventdalen, some outer and drier parts of the river terraces, with an eolian cover, do not exhibit the same magnitude of seasonal subsidence and heave as the lower parts of the fans/terraces ([Figs. 3, 4 and 6](#)). This makes sense, as the water content is generally lower in the outer river terraces than in the lower alluvial fans ([Cable et al., 2018](#)).

The 2D InSAR displacement rates for different geomorphological units overlap significantly ([Fig. 8](#)), which makes direct classification impossible, as also discussed by [Eckerstorfer et al. \(2018\)](#). The effect of the different spatial resolutions, the georeferencing inaccuracy, the simplification of the geomorphological units and the mapping scale partially explain the overlaps. For example, the delineation of 'Alluvial sediment, pre-recent', 'Alluvial sediment, recent' and 'Fluvial sediment' units in highly dynamic valley bottoms is subject to inaccuracies. 'Terminal and medial moraine' also includes debris-covered glaciers and 'Anthropogenic material' includes both infrastructure in valley bottoms and mining deposits creeping on slopes. In addition, the complex behaviours under investigation imply that different processes can have similar displacement rates, or that similar processes under variable environmental contexts can have different rates. Jointly analysing vertical and horizontal components determined from the 2D InSAR method allows, however, for more valuable information to differentiate sediments, bedrock and landforms ([Figs. 9, 10 and S12](#)). Without additional information, a completely automatic processing of InSAR displacements for mapping geomorphology remains unfeasible, but the findings highlight the potential of using InSAR to refine the inventory and delineation of specific landforms on existing maps, or as a supporting tool for geomorphological or geocryological mapping, as the spatial distribution of InSAR displacements is related to the distribution of frost-susceptible sediments and the variability of water content available for ground ice formation in the active layer. When used in combination with other environmental information such as topography, geology, climate, vegetation and/or hydrology, InSAR may also be valuably integrated into statistically-based geomorphological distribution modelling ([Hjort and Luoto, 2013](#)).

## 5.3. InSAR contribution for investigation of ground thermal conditions

With the increase of repeat-pass frequency of recent SAR satellites such as S1, InSAR can be used to monitor the temporal variations of ground displacements at seasonal scale. This has direct applications like in geohazard studies, but can also provide indirect findings. Our results show that there is a clear correspondence between active layer thermal regime and the InSAR measured displacements at the location of two boreholes, with the timing of the subsidence and heave onsets matching the observed ground surface and active layer thawing and freezing ([Fig. 11](#)). This confirms that InSAR can be a valuable tool for the indirect monitoring of active layer dynamics over landforms dominated by subsidence and heave patterns, as in the flat bottom of Adventdalen or on gentle solifluction slopes in Endalen. In high-relief contexts where the processes are mainly gravity-driven, InSAR can provide information

about the temporal variability of the creep velocity ([Fig. 7](#)), but the time series have to be interpreted carefully due to the complex orientation of the real displacements and their relations with the LOS measurements.

In the lowlands, previous research has studied and modelled the relationship between InSAR time series and active layer dynamics, often with the objective of exploiting InSAR for ALT retrieval. The Stefan equation ([Stefan, 1891](#)) allows for a simple calculation of the development of thaw depth through the season, based on the accumulated thawing-degree days derived from air temperature. Assuming homogenous ground, a defined amount of ground ice and that all pore ice turns into water during the thawing, the InSAR-measured subsidence can be converted into thaw depth ([Liu et al., 2012](#)). More recent models combine the use of thawing and freezing indices to more realistically depict short term variations and take into account eventual transient summer freezing ([Hu et al., 2018](#)) or investigate how other climatic factors such as precipitation affect the ground surface dynamics ([Zhao et al., 2016](#)).

These models can perform well in homogenous areas and their simplicity is valuable for upscaling investigations in permafrost areas, where little additional data is available. However, they also have some limitations. Major elements besides climatic variables are often neglected. Our results show that the displacement magnitude and timing are geomorphologically-controlled, largely determined by the sediment, bedrock or landform types, and thus cannot be explained only by climatic variables. Other variables have to be considered, such as the heterogeneity of the ground properties and the water available for ground ice formation in the active layer ([Shiklomanov et al., 2010](#)), as well as the presence of different ice types in the ground (e.g. pore and segregated ice) and the factors controlling ice lens formation ([Rempel, 2007](#)). Both elements impact the ground thermal regime (e.g. due to porosity, thermal conductivity, release/absorption of latent heat of fusion of water) and how the surface is affected by a phase change (e.g. due to melting of ice lenses vs. pore ice only). Comparing InSAR results to field data, [Daout et al. \(2017\)](#) showed that the magnitude and timing of the ground displacement patterns are controlled by ground properties and water availability. Their conclusions from the Tibet Plateau concur with our findings which suggest that, especially in complex periglacial landscapes encompassing a wide range of topographical, geomorphological and hydrological conditions, InSAR is a valuable tool for the investigation of freeze and thaw processes at large scale, but may benefit from further combination with in situ data and modelling techniques.

## 6. Conclusion

Our study demonstrates the value of multi-sensor and multi-geometry InSAR for investigating complex permafrost landscapes containing both high-relief and lowlands. The analysis of the spatial variability of ground displacement rates based on decomposed vertical and east-west horizontal TerraSAR-X InSAR results compared to a simplified geomorphological map show that it is possible to identify specific 2D displacement patterns for different geomorphological units. In the flat valley bottoms, thaw subsidence is detected and the magnitude varies according to the water availability and frost-susceptibility of the sediments. On valley slopes, downslope displacements combining vertical and horizontal components are detected and their magnitude varies depending on the involved creep process. Based on 6-month continuous time series from Sentinel-1 in June–December 2017, we were able to correctly identify ground displacement variations related to active layer thawing and freezing over flat or low-inclined slopes, where the seasonal change from thaw subsidence to frost heave dominates the displacement pattern. Through comparison with in situ ground temperature measurements in the active layer, we show that the timing of the InSAR seasonal subsidence and heave patterns matches the ground thawing and freezing periods measured in two boreholes.

The identified spatio-temporal relations between ground surface displacements and environmental variables evidence the potential for further exploitation of InSAR technology for understanding, mapping and monitoring the dynamics of remote periglacial landscapes. The findings support the development of more advanced models to remotely and indirectly retrieve variables related to permafrost such as active layer thickness, which is one of the two Essential Climate Variables for permafrost.

## Acknowledgements

Line Rouyet's PhD study is part of the research project FrostInSAR (2017–2021) funded by the Space Programme of the Research Council of Norway (Project Nr: 263005). The development of the GSAR processing chain and previous research applying InSAR in periglacial environments have been supported by the Norwegian Space Centre, the Research Council of Norway (Project Nr: 212022) and the European Space Agency (Project Nr: 4000106830 and 4000119115). TerraSAR-X scenes were provided by the German Aerospace Center (DLR) under the TSX-AO project contracts #GEO0565 and #GEO3519. Sentinel-1 scenes were provided as part of the EU Copernicus data service (2015–2017). We acknowledge the work and valuable feedback from three anonymous reviewers and the editor Prof. Dar Roberts who contributed to improve the manuscript. We thank Markus Eckerstorfer for his contribution to the previous PermaSAT and PermaSAR projects that led to the initiation of the current FrostInSAR project. We are grateful for the interest and inputs of Stefanie Cable shared during various discussions. We acknowledge the work of the ESA GlobPermafrost and CCI+Permafrost initiatives providing a great international framework and inspiration for research on remote sensing of permafrost landscapes.

## Appendix A. Supplementary data

Supplementary data to this article can be found online at <https://doi.org/10.1016/j.rse.2019.111236>.

## References

- André, M.F., 1995. Holocene climate fluctuations and geomorphic impact of extreme events in Svalbard. *Geografiska Annaler: Series A, Physical Geography* 77 (4), 241–250. <https://doi.org/10.1080/04353676.1995.11880444>.
- Antonova, S., Sudhaus, H., Strozzi, T., Zwieback, S., Kääh, A., Heim, B., Langer, M., Bornemann, N., Boike, J., 2018. Thaw subsidence of a Yedoma landscape in northern Siberia, measured in situ and estimated from TerraSAR-X interferometry. *Remote Sens. Environ.* 10 (4), 494. <https://doi.org/10.3390/rs10040494>.
- Baran, I., Stewart, M.P., Kampes, B.M., Perski, Z., Lilly, P., 2003. A modification to the Goldstein radar interferogram filter. *IEEE Trans. Geosci. Remote Sens.* 41 (9), 2114–2118. <https://doi.org/10.1109/TGRS.2003.817212>.
- Barboux, C., Delaloye, R., Lambiel, C., 2014. Inventorying slope movements in an Alpine environment using DInSAR. *Earth Surf. Process. Landf.* 39 (15), 2087–2099. <https://doi.org/10.1002/esp.3603>.
- Barboux, C., Strozzi, T., Delaloye, R., Wegmüller, U., Collet, C., 2015. Mapping slope movements in Alpine environments using TerraSAR-X interferometric methods. *ISPRS J. Photogramm. Remote Sens.* 109, 178–192. <https://doi.org/10.1016/j.isprsjprs.2015.09.010>.
- Bartsch, A., Grosse, G., Kääh, A., Westermann, S., Strozzi, T., Wiesmann, A., Duguay, C., Seifert, F.M., Obu, J., Goler, R., 2016. GlobPermafrost – how space-based earth observation supports understanding of permafrost. In: *Proc. Living Planet Symposium 2016, Prague, Czech Republic, 9–13 May 2016*. vol. 740. pp. 332.
- Berardino, P., Fornaro, G., Lanari, R., Sansosti, E., 2002. A new algorithm for surface deformation monitoring based on small baseline differential SAR interferograms. *IEEE Trans. Geosci. Remote Sens.* 40 (11), 2375–2383. <https://doi.org/10.1109/TGRS.2002.803792>.
- Blikra, L.H., Christiansen, H.H., 2014. A field-based model of permafrost-controlled rockslide deformation in northern Norway. *Geomorphology* 208, 34–49. <https://doi.org/10.1016/j.geomorph.2013.11.014>.
- Cable, S., Elberling, B., Kroon, A., 2018. Holocene permafrost history and cryostratigraphy in the High-Arctic Adventdalen Valley, central Svalbard. *Boreas* 47 (2), 423–442. <https://doi.org/10.1111/bor.12286>.
- Cavalié, O., Doin, M.P., Lasserre, C., Briole, P., 2007. Ground motion measurement in the Lake Mead area, Nevada, by differential synthetic aperture radar interferometry time series analysis: probing the lithosphere rheological structure. *Journal of Geophysical Research: Solid Earth* (B3), 112. <https://doi.org/10.1029/2006JB004344>.
- Chen, C., Zebker, H.A., 2002. Phase unwrapping for large SAR interferograms: statistical segmentation and generalized network models. *IEEE Trans. Geosci. Remote Sens.* 40 (8), 1709–1719. <https://doi.org/10.1109/TGRS.2002.802453>.
- Christiansen, H., Humlum, O., 2008. Interannual variations in active layer thickness in Svalbard. In: *Proc. Ninth International Conference on Permafrost, Fairbanks, Alaska, U.S.A., 29 June–3 July*, pp. 257–262.
- Christiansen, H.H., Eitzelmüller, B., Isaksen, K., Juliussen, H., Farbrøt, H., Humlum, O., Johansson, M., Ingeman-Nielsen, T., Kristensen, L., Hjort, J., Holmlund, P., Sannel, A.B.K., Sigsgaard, C., Åkerman, H.J., Foged, N., Blikra, L.H., Pernosky, M.A., Ødegård, R.S., 2010. The thermal state of permafrost in the nordic area during the international polar year 2007–2009. *Permafrost. Periglac. Process.* 21 (2), 156–181. <https://doi.org/10.1002/ppp.687>.
- Christiansen, H.H., Humlum, O., Eckerstorfer, M., 2013. Central Svalbard 2000–2011 meteorological dynamics and periglacial landscape response. *Arct. Antarct. Alp. Res.* 45 (1), 6–18. <https://doi.org/10.1657/1938-4246-45.16>.
- Dallmann, W.K., Kjærnet, T., Nøttvedt, A., 2001. *Geological Map of Svalbard 1:100,000. Sheet C9G Adventdalen (Text)*. Norwegian Polar Institute (Temakart No. 31/32).
- Daout, S., Doin, M.P., Peltzer, G., Socquet, A., Lasserre, C., 2017. Large-scale InSAR monitoring of permafrost freeze-thaw cycles on the Tibetan Plateau. *Geophys. Res. Lett.* 44 (2), 901–909. <https://doi.org/10.1002/2016GL070781>.
- De Zan, F., Parizzi, A., Prats-Iraola, P., López-Dekker, P., 2014. A SAR interferometric model for soil moisture. *IEEE Trans. Geosci. Remote Sens.* 52 (1), 418–425. <https://doi.org/10.1109/TGRS.2013.2241069>.
- Delaloye, R., Lambiel, C., Lugon, R., Raetz, H., Strozzi, T., 2007. Typical ERS InSAR signature of slope movements in a periglacial mountain environment (Swiss Alps). In: *Proc. ENVISAT Symposium 2007, Montreux, Switzerland, 23–27 April 2007, ESA SP-636*.
- Delaloye, R., Lambiel, C., Gärtner-Roer, I., 2010. Overview of rock glacier kinematics research in the Swiss Alps. *Geographica Helvetica* 65, 135–145. <https://doi.org/10.5194/ggh-65-135-2010>. 2010.
- Eckerstorfer, M., Christiansen, H.H., Vogel, S., Rubensdotter, L., 2013. Snow cornice dynamics as a control on plateau edge erosion in central Svalbard. *Earth Surf. Process. Landf.* 38 (5), 466–476. <https://doi.org/10.1002/esp.3292>.
- Eckerstorfer, M., Eriksen, H.Ø., Rouyet, L., Christiansen, H.H., Lauknes, T.R., Blikra, L.H., 2018. Comparison of geomorphological field mapping and 2D-InSAR mapping of periglacial landscape activity at Nordnesfjellet, northern Norway. *Earth Surf. Process. Landf.* 43 (10), 2147–2156. <https://doi.org/10.1002/esp.4380>.
- Emardson, T.R., Simons, M., Webb, F.H., 2003. Neutral atmospheric delay in interferometric synthetic aperture radar applications: statistical description and mitigation. *Journal of Geophysical Research: Solid Earth* 108 (B5), 2231. <https://doi.org/10.1029/2002JB001781>.
- Eriksen, H.Ø., Lauknes, T.R., Larsen, Y., Corner, G.D., Bergh, S.G., Dehls, J., Kierulf, H.P., 2017. Visualizing and interpreting surface displacement patterns on unstable slopes using multi-geometry satellite SAR interferometry (2D InSAR). *Remote Sens. Environ.* 191, 297–312. <https://doi.org/10.1016/j.rse.2016.12.024>.
- Eriksen, H.Ø., Rouyet, L., Lauknes, T.R., Berthling, I., Isaksen, K., Hindberg, H., Larsen, Y., Corner, G.D., 2018. Recent acceleration of a rock glacier complex, Ådjet, Norway, documented by 62 years of remote sensing observations. *Geophys. Res. Lett.* 45 (16), 8314–8323. <https://doi.org/10.1029/2018GL077605>.
- Eitzelmüller, B., Schuler, T.V., Isaksen, K., Christiansen, H.H., Farbrøt, H., Benestad, R., 2011. Modeling the temperature evolution of Svalbard permafrost during the 20th and 21st century. *Cryosphere* 5 (1), 67. <https://doi.org/10.5194/tc-5-67-2011>.
- Førland, E.J., Benestad, R., Hanssen-Bauer, I., Haugen, J.E., Skaugen, T.E., 2011. Temperature and precipitation development at Svalbard 1900–2100. *Adv. Meteorol.* 2011. <https://doi.org/10.1155/2011/893790>.
- French, H.M., 2007. *The Periglacial Environment, Third edition*. John Wiley & Sons, Chichester, England.
- Gabriel, A.K., Goldstein, R.M., Zebker, H.A., 1989. Mapping small elevation changes over large areas: differential radar interferometry. *Journal of Geophysical Research: Solid Earth* 94 (B7), 9183–9191. <https://doi.org/10.1029/JB094iB07p09183>.
- Gilbert, G.L., O'Neill, H.B., Nemecek, W., Thiel, C., Christiansen, H.H., Buyllaert, J.P., 2018. Late Quaternary sedimentation and permafrost development in a Svalbard fjord-valley, Norwegian high Arctic. *Sedimentology*. <https://doi.org/10.1111/sed.12476>.
- Goldstein, R.M., Werner, C.L., 1998. Radar interferogram filtering for geophysical applications. *Geophys. Res. Lett.* 25 (21), 4035–4038. <https://doi.org/10.1029/1998GL900033>.
- Haerberli, W., Hallet, B., Arenson, L., Elconin, R., Humlum, O., Kääh, A., Kaufmann, V., Ladanyi, B., Matsuoka, N., Springman, S., Mühl, D.V., 2006. Permafrost creep and rock glacier dynamics. *Permafrost. Periglac. Process.* 17 (3), 189–214. <https://doi.org/10.1002/ppp.561>.
- Harris, C., Davies, M.C., Coutard, J.P., 1995. Laboratory simulation of periglacial solifluction: significance of porewater pressures, moisture contents and undrained shear strengths during soil thawing. *Permafrost. Periglac. Process.* 6 (4), 293–311. <https://doi.org/10.1002/ppp.3430060403>.
- Harris, C., Arenson, L.U., Christiansen, H.H., Eitzelmüller, B., Frauenfelder, R., Gruber, S., Haerberli, W., Hauck, C., Hölzle, M., Humlum, O., Isaksen, K., Kääh, A., Kern-Lütschg, M.A., Lehning, M., Matsuoka, N., Murton, J.B., Nötzli, J., Phillips, M., Ross, N., Seppälä, M., Springman, S.M., Von der Mühl, D., 2009. Permafrost and climate in Europe: monitoring and modelling thermal, geomorphological and geotechnical responses. *Earth Sci. Rev.* 92 (3–4), 117–171. <https://doi.org/10.1016/j.earscirev.2008.12.002>.
- Harris, C., Kern-Lütschg, M.A., Christiansen, H.H., Smith, F., 2011. The role of inter-annual climate variability in controlling solifluction processes, Endalen, Svalbard. *Permafrost. Periglac. Process.* 22 (3), 239–253. <https://doi.org/10.1002/ppp.727>.
- Härtel, S., Christiansen, H.H., 2014. *Geomorphological and Cryological map of Adventdalen, Svalbard*. PANGAEA. <https://doi.org/10.1594/PANGAEA.833048>.
- Hjort, J., Luoto, M., 2013. Statistical methods for geomorphic distribution modeling. In: Schroder, J. (Editor in Chief), Baas, A.C.W. (Eds.), *Treatise on Geomorphology. Quantitative Modeling of Geomorphology*, vol. 2. Academic Press, San Diego, pp. 59–73. <https://doi.org/10.1016/B978-0-12-374739-6.00028-2>.
- Hu, Y., Liu, L., Larson, K.M., Schaefer, K.M., Zhang, J., Yao, Y., 2018. GPS interferometric reflectometry reveals cyclic elevation changes in thaw and freezing seasons in a permafrost area (Barrow, Alaska). *Geophys. Res. Lett.* 45, 5581–5589. <https://doi.org/10.1029/2017GL075000>.

- org/10.1029/2018GL077960.
- Humlum, O., 2000. The geomorphic significance of rock glaciers: estimates of rock glacier debris volumes and headwall recession rates in West Greenland. *Geomorphology* 35 (1–2), 41–67. [https://doi.org/10.1016/S0169-555X\(00\)00022-2](https://doi.org/10.1016/S0169-555X(00)00022-2).
- Humlum, O., Instanes, A., Sollid, J.L., 2003. Permafrost in Svalbard: a review of research history, climatic background and engineering challenges. *Polar Res.* 22 (2), 191–215. <https://doi.org/10.3402/polar.v22i2.6455>.
- Isaksen, K., Christiansen, H.H., Westermann, S., 2019. 7.1 permafrost temperature and active layer thickness. In: Hanssen-Bauer, I., Førland, E.J., Hisdal, H., Mayer, S., Sandø, A.B., Sorteberg, A. (Eds.), *Climate in Svalbard 2100*, pp. 105–110 NCCS report no 1/2019.
- Kenyi, L.W., Kaufmann, V., 2001. Estimation of alpine permafrost surface deformation using InSAR data. In: Proc. Geoscience and Remote Sensing Symposium, IGARSS'01, Sydney, Australia, 9–13 July 2001. vol. 3. IEEE 2001 International, pp. 1107–1109. <https://doi.org/10.1109/IGARSS.2001.976761>.
- Larsen, Y., Engen, G., Lauknes, T.R., Malnes, E., Høgda, K.A., 2005. A generic differential interferometric SAR processing system, with applications to land subsidence and snow-water equivalent retrieval. In: Proc. Fringe 2005 Workshop, Frascati, Italy, 28 November–2 December 2005. vol. 61 (ESA SP-610).
- Lauknes, T.R., 2011. InSAR tropospheric stratification delays: correction using a small baseline approach. *IEEE Geosci. Remote Sens. Lett.* 8 (6), 1070–1074. <https://doi.org/10.1109/LGRS.2011.2156381>.
- Lauknes, T.R., Zebker, H.A., Larsen, Y., 2011. InSAR deformation time series using an L1-norm small-baseline approach. *IEEE Geosci. Remote Sens.* 49 (1), 536–546. <https://doi.org/10.1109/TGRS.2010.2051951>.
- Liu, L., Schaefer, K., Zhang, T., Wahr, J., 2012. Estimating 1992–2000 average active layer thickness on the Alaskan North Slope from remotely sensed surface subsidence. *Journal of Geophysical Research: Earth Surface* 117 (F1). <https://doi.org/10.1029/2011JF002041>.
- Lyons, S., Sandwell, D., 2003. Fault creep along the southern San Andreas from interferometric synthetic aperture radar, permanent scatterers, and stacking. *Journal of Geophysical Research: Solid Earth* 108 (B1). <https://doi.org/10.1029/2002JB001831>.
- Major, H., Haremo, W.K., Dallmann, W.K., Andresen, A., 2001. *Geological Map of Svalbard 1:100,000. Sheet C9G Adventdalen (Map)*. Norwegian Polar Institute (Temarkart No. 31/32).
- Massonet, D., Feigl, K.L., 1998. Radar interferometry and its application to changes in the earth's surface. *Rev. Geophys.* 36 (4), 441–500. <https://doi.org/10.1029/97RG03139>.
- Matsuoka, N., 2001. Solifluction rates, processes and landforms: a global review. *Earth Sci. Rev.* 55 (1–2), 107–134. [https://doi.org/10.1016/S0012-8252\(01\)00057-5](https://doi.org/10.1016/S0012-8252(01)00057-5).
- Matsuoka, N., Abe, M., Ijiri, M., 2003. Differential frost heave and sorted patterned ground: field measurements and a laboratory experiment. *Geomorphology* 52 (1–2), 73–85. [https://doi.org/10.1016/S0169-555X\(02\)00249-0](https://doi.org/10.1016/S0169-555X(02)00249-0).
- Nelson, F.E., Shiklomanov, N.I., Mueller, G.R., Hinkel, K.M., Walker, D.A., Bockheim, J.G., 1997. Estimating active-layer thickness over a large region: Kuparuk River basin, Alaska, USA. *Arct. Alp. Res.* 29 (4), 367–378. <https://doi.org/10.1080/00040851.1997.12003258>.
- Nelson, F.E., Anisimov, O.A., Shiklomanov, N.I., 2002. Climate change and hazard zonation in the circum-Arctic permafrost regions. *Nat. Hazards* 26 (3), 203–225. <https://doi.org/10.1023/A:1015612918401>.
- Norwegian Polar Institute, 2014a. Terrenngmodell Svalbard (S0 Terrenngmodell). Norwegian Polar Institute. [10.21334/npolar.2014.dce53a47](https://doi.org/10.21334/npolar.2014.dce53a47).
- Norwegian Polar Institute, 2014b. Kartdata Svalbard 1:100 000 (S100 Kartdata)/Map Data. Norwegian Polar Institute. [10.21334/npolar.2014.645336c7](https://doi.org/10.21334/npolar.2014.645336c7).
- Peel, M.C., Finlayson, B.L., McMahon, T.A., 2007. Updated world map of the Köppen-Geiger climate classification. *Hydrol. Earth Syst. Sci. Discuss.* 4 (2), 439–473. <https://doi.org/10.5194/hess-11-1633-2007>.
- Peltzer, G., Crampé, F., Hensley, S., Rosen, P., 2001. Transient strain accumulation and fault interaction in the Eastern California shear zone. *Geology* 29 (11), 975–978. [https://doi.org/10.1130/0091-7613\(2001\)029<0975:TSAAFI>2.0.CO;2](https://doi.org/10.1130/0091-7613(2001)029<0975:TSAAFI>2.0.CO;2).
- Rempel, A.W., 2007. Formation of ice lenses and frost heave. *Journal of Geophysical Research: Earth Surface* (F2), 112. <https://doi.org/10.1029/2006JF000525>.
- Rignot, E., Hallet, B., Fountain, A., 2002. Rock glacier surface motion in Beacon Valley, Antarctica, from synthetic aperture radar interferometry. *Geophys. Res. Lett.* 29 (12). <https://doi.org/10.1029/2001GL013494>.
- Romanovsky, V.E., Marchenko, S.S., Daanen, R., Sergeev, D.O., Walker, D.A., 2008. Soil climate and frost heave along the permafrost/ecological North American Arctic transect. In: Proc. Ninth International Conference on Permafrost 2005, Fairbanks, U.S.A. vol. 2. pp. 1519–1524.
- Romanovsky, V.E., Smith, S.L., Christiansen, H.H., 2010. Permafrost thermal state in the polar Northern Hemisphere during the international polar year 2007–2009: a synthesis. *Permafr. Periglac. Process.* 21 (2), 106–116. <https://doi.org/10.1002/ppp.689>.
- Rudy, A.C., Lamoureux, S.F., Treitz, P., Short, N., Brisco, B., 2018. Seasonal and multi-year surface displacements measured by DInSAR in a High Arctic permafrost environment. *Int. J. Appl. Earth Obs. Geoinf.* 64, 51–61. <https://doi.org/10.1016/j.jag.2017.09.002>.
- Rykhov, R.P., Lu, Z., 2008. InSAR detects possible thaw settlement in the Alaskan Arctic Coastal Plain. *Can. J. Remote. Sens.* 34 (2), 100–112. <https://doi.org/10.5589/m08-018>.
- Sandwell, D.T., Price, E.J., 1998. Phase gradient approach to stacking interferograms. *Journal of Geophysical Research: Solid Earth* 103 (B12), 30183–30204. <https://doi.org/10.1029/1998JB900008>.
- Schaefer, K., Liu, L., Parsekian, A., Jafarov, E., Chen, A., Zhang, T., Gusmeroli, A., Panda, S., Zebker, H.A., Schaefer, T., 2015. Remotely sensed active layer thickness (ReSALT) at Barrow, Alaska using interferometric synthetic aperture radar. *Remote Sens.* 7 (4), 3735–3759. <https://doi.org/10.3390/rs70403735>.
- Schuh, C., Frampton, A., Christiansen, H.H., 2017. Soil moisture redistribution and its effect on inter-annual active layer temperature and thickness variations in a dry loess terrace in Adventdalen, Svalbard. *Cryosphere* 11 (1), 635. <https://doi.org/10.5194/11-635-2017>.
- Shiklomanov, N.I., Streletskiy, D.A., Nelson, F.E., Hollister, R.D., Romanovsky, V.E., Tweedie, C.E., Bockheim, J.G., Brown, J., 2010. Decadal variations of active-layer thickness in moisture-controlled landscapes, Barrow, Alaska. *Journal of Geophysical Research: Biogeosciences* 115 (G4). <https://doi.org/10.1029/2009JG001248>.
- Shiklomanov, N.I., Streletskiy, D.A., Nelson, F.E., 2012. Northern hemisphere component of the global circumpolar active layer monitoring (CALM) program. In: Proc. 10th Int. Conf. on Permafrost, Salekhard, Russia, 25–29 June. vol. 1. pp. 377–382.
- Short, N., LeBlanc, A.M., Sladen, W., Oldenborger, G., Mathon-Dufour, V., Brisco, B., 2014. RADARSAT-2 D-InSAR for ground displacement in permafrost terrain, validation from Iqaluit Airport, Baffin Island, Canada. *Remote Sens. Environ.* 141, 40–51. <https://doi.org/10.1016/j.rse.2013.10.016>.
- Shur, Y., Hinkel, K.M., Nelson, F.E., 2005. The transient layer: implications for cryology and climate-change science. *Permafr. Periglac. Process.* 16 (1), 5–17. <https://doi.org/10.1002/ppp.518>.
- Smith, M.W., 1985. Observations of soil freezing and frost heave at Inuvik, Northwest Territories, Canada. *Can. J. Earth Sci.* 22 (2), 282–290. <https://doi.org/10.1139/e85-024>.
- Sørbel, L., Tolgensbakk, J., Hagne, O., Høgvard, K., 2001. *Geomorphological and Quaternary Geological Map of Svalbard 1:100,000. Sheet C9Q Adventdalen (Map)*. Norwegian Polar Institute (Temarkart No. 31/32).
- Stefan, J., 1891. Über die Theorie der Eisbildung, insbesondere über die Eisbildung im Polarmeere. *Ann. Phys.* 278 (2), 269–286. <https://doi.org/10.1002/andp.18912780206>.
- Strozzi, T., Kääh, A., Frauenfelder, R., 2004. Detecting and quantifying mountain permafrost creep from in situ inventory, space-borne radar interferometry and airborne digital photogrammetry. *Int. J. Remote Sens.* 25 (15), 2919–2931. <https://doi.org/10.1080/0143116042000192330>.
- Strozzi, T., Delaloye, R., Kääh, A., Ambrosi, C., Perruchoud, E., Wegmüller, U., 2010. Combined observations of rock mass movements using satellite SAR interferometry, differential GPS, airborne digital photogrammetry, and airborne photography interpretation. *Journal of Geophysical Research: Earth Surface* 115 (F1). <https://doi.org/10.1029/2009JF001311>.
- Strozzi, T., Antonova, S., Günther, F., Mätzler, E., Vieira, G., Wegmüller, U., Westermann, S., Bartsch, A., 2018. Sentinel-1 SAR interferometry for surface deformation monitoring in low-land permafrost areas. *Remote Sens.* 10, 1360. <https://doi.org/10.3390/rs10091360>.
- Tolgensbakk, J., Sørbel, L., Høgvard, K., 2001. *Geomorphological and Quaternary Geological Map of Svalbard 1:100,000. Sheet C9Q Adventdalen (Text)*. Norwegian Polar Institute (Temarkart No. 31/32).
- Trofaier, A.M., Westermann, S., Bartsch, A., 2017. Progress in space-borne studies of permafrost for climate science: towards a multi-ECV approach. *Remote Sens. Environ.* 203, 55–70. <https://doi.org/10.1016/j.rse.2017.05.021>.
- Tymofeyeva, E., Fialko, Y., 2015. Mitigation of atmospheric phase delays in InSAR data, with application to the eastern California shear zone. *Journal of Geophysical Research: Solid Earth* 120 (8), 5952–5963. <https://doi.org/10.1002/2015JB011886>.
- Wang, Z., Li, S., 1999. Detection of winter frost heaving of the active layer of Arctic permafrost using SAR differential interferograms. In: Proc. Geoscience and Remote Sensing Symposium, IGARSS'99, Hamburg, Germany, 28 June–2 July 1999. IEEE 1999 International. vol. 4. pp. 1946–1948. <https://doi.org/10.1109/IGARSS.1999.774995>.
- Wang, C., Zhang, Z., Zhang, H., Wu, Q., Zhang, B., Tang, Y., 2017. Seasonal deformation features on Qinghai-Tibet railway observed using time-series InSAR technique with high-resolution TerraSAR-X images. *Remote Sensing Letters* 8 (1), 1–10. <https://doi.org/10.1080/2150704X.2016.1225170>.
- Wolfe, S.A., Short, N.H., Morse, P.D., Schwarz, S.H., Stevens, C.W., 2014. Evaluation of RADARSAT-2 DInSAR seasonal surface displacement in discontinuous permafrost terrain, Yellowknife, Northwest Territories, Canada. *Can. J. Remote. Sens.* 40 (6), 406–422. <https://doi.org/10.1080/07038992.2014.1012836>.
- Zhang, T., Barry, R.G., Knowles, K., Ling, F., Armstrong, R.L., 2003. Distribution of seasonally and perennially frozen ground in the Northern Hemisphere. In: Proc. 8th International Conference on Permafrost, Zürich, Switzerland, 21–25 July. vol. 2. AA Balkema Publishers, pp. 1289–1294.
- Zhang, Y., Michalowski, R.L., 2015. Thermal-hydro-mechanical analysis of frost heave and thaw settlement. *J. Geotech. Geoenviron.* 141 (7), 04015027. [https://doi.org/10.1061/\(ASCE\)GT.1943-5606.0001305](https://doi.org/10.1061/(ASCE)GT.1943-5606.0001305).
- Zhao, L., Cheng, G., Li, S., Zhao, X., Wang, S., 2000. Thawing and freezing processes of active layer in Wudaoliang region of Tibetan Plateau. *Chin. Sci. Bull.* 45 (23), 2181–2187.
- Zhao, R., Li, Z.W., Feng, G.C., Wang, Q.J., Hu, J., 2016. Monitoring surface deformation over permafrost with an improved SBAS-InSAR algorithm: with emphasis on climatic factors modeling. *Remote Sens. Environ.* 184, 276–287. <https://doi.org/10.1016/j.rse.2016.07.019>.
- Zwieback, S., Hensley, S., Hajnsek, I., 2017. Soil moisture estimation using differential radar interferometry: toward separating soil moisture and displacements. *IEEE Trans. Geosci. Remote Sens.* 55 (9), 5069–5083. <https://doi.org/10.1109/TGRS.2017.2702099>.